

Minimum-entropy constraints on galactic potentials

LEANDRO BERALDO E SILVA ^{1,2} MONICA VALLURI ¹ EUGENE VASILIEV ³ KOHEI HATTORI ^{4,5,1}
WALTER DE SIQUEIRA PEDRA,⁶ AND KATHRYNE J. DANIEL ²

¹*Department of Astronomy and Astrophysics, University of Michigan, Ann Arbor, MI, USA*

²*Steward Observatory and Department of Astronomy,*

University of Arizona, 933 N. Cherry Ave., Tucson, AZ 85721, USA

³*University of Surrey, Guildford, Surrey GU2 7XH, United Kingdom*

⁴*National Astronomical Observatory of Japan, 2-21-1 Osawa, Mitaka, Tokyo 181-8588, Japan*

⁵*The Institute of Statistical Mathematics, 10-3 Midoricho, Tachikawa, Tokyo 190-8562, Japan*

⁶*University of São Paulo, Institute of Mathematics and Computer Sciences, Av. Trab. São Carlense 400, 13566-590, São Carlos, SP, Brazil*

ABSTRACT

A tracer sample in a gravitational potential, starting from a generic initial condition, phase-mixes towards a stationary state. This evolution is accompanied by an entropy increase, and the final state is characterized by a distribution function (DF) that depends only on integrals of motion (Jeans theorem). In terms of angle-action variables, the final state is uniform in angles (high entropy) and maximally clustered in actions (low entropy). We present a method exploring this fact to constrain a gravitational potential using a sample that is stationary in it. We estimate the entropy in the action space of trial potentials and recover the true potential by minimizing this entropy. This method avoids assuming a known DF, and may be applicable to other sets of integrals. We provide expressions for the entropy of DFs depending on energy, $f(E)$, energy and angular momentum, $f(E, L)$, or three actions, $f(\vec{J})$, and investigate the bias and fluctuations in their estimates. We show that the method correctly recovers the potential parameters for spherical and axisymmetric potentials. We also present a methodology to characterize the posterior probability distribution of the parameters with an Approximate Bayesian Computation, and indicate a pathway for application to observational data. Using $N = 10^4$ tracers with 20%-uncertainties in the 6D coordinates, we recover the flattening parameter q of an axisymmetric potential with $\sigma_q/q \sim 10\%$.

Keywords: Galactic dynamics — Dark matter — Milky Way halo

1. INTRODUCTION

The gravitational potential is a fundamental aspect of any galaxy. It determines the orbits of its individual stars and, after all, the light distribution we observe in optical images of all kinds of galaxies. In the case of the Milky Way (MW), we can nowadays precisely measure 6D coordinates for millions of stars with Gaia (Gaia Collaboration et al. 2016) in combination with spectroscopic surveys such as APOGEE (Majewski et al. 2017), LAMOST (Cui et al. 2012), GALAH (De Silva et al. 2015) and DESI-MWS (Cooper et al. 2023). With theoretical

modeling, this wealth of data can be translated into a detailed picture of the Galaxy’s mass distribution.

Of particular interest is the characterization of MW’s dark matter (DM) halo shape, which may provide constraints on different scenarios for its composition (see e.g. Valluri et al. 2022). Since this component is not directly observed, one needs to infer its mass distribution from the spatial distribution and kinematics of stars. Several methods have been developed to recover the underlying potential using a tracer population. A non-exhaustive list includes the virial theorem and its variants (Zwicky 1933; Bahcall & Tremaine 1981; Watkins et al. 2010), the “orbital roulette” (Beloborodov & Levin 2004), the marginalization over an arbitrary number of distribution function (DF) compo-

nents (Magorrian 2014), the generating-function method of Tremaine (2018), the minimization of the entropy of tidal streams (Peñarrubia et al. 2012; Sanderson et al. 2015), the “orbital pdf” method of Han et al. (2016) and the Maximum-Likelihood method for DF fitting (e.g. McMillan & Binney 2012, 2013; Deason et al. 2021).

In all these methods, further assumptions are required besides the information contained in the observed dataset. For instance, for tracers described by a DF, one needs to assume that these tracers constitute a system in dynamical equilibrium. Otherwise, any potential is consistent with a DF describing a non-stationary system (McMillan & Binney 2012; Green et al. 2023). As another example, when modeling tidal streams, the equilibrium assumption is replaced by an equally strong one, that the debris were initially localized in phase space.

From the Jeans theorem, the DF of a system in equilibrium can be written as a function of integrals of motion only, reducing the 6D phase-space to 3D or less (Binney & Tremaine 2008). For instance, isotropic spherical systems can be described by a DF $f = f(E)$, where E is the star’s energy, while for anisotropic spherical systems we can assume $f = f(E, L)$, where L is the magnitude of the angular momentum. In general, samples in realistic galactic potentials normally require three integrals of motion. In practice, this dimension reduction is fundamental for a more efficient use of data.

A DF depending on less integrals of motion than required, i.e. a dimension reduction too severe, delivers incorrect results. On the other hand, one can assume a DF depending on more integrals than required, but this is not the most efficient use of the data since it does not reduce the dimensionality as much as one could do. Thus, adopting three integrals is generally a good compromise between generality and efficiency.

Among all integrals of motion, actions offer several advantages (despite the difficulties in estimating them in practice – see e.g. Sanders & Binney 2016): the transformation from phase-space coordinates (\vec{r}, \vec{v}) to angle-action coordinates $(\vec{\theta}, \vec{J})$ is canonical, thus $d\vec{r}d\vec{v} = d\vec{\theta}d\vec{J}$; actions are adiabatic invariants, i.e. they are conserved under slow changes in the potential; angles are restricted to $[0, 2\pi)$, and a system in equilibrium (phase-mixed) is simply described by a probability density function (**pdf**)¹ in action space $F(\vec{J}) = (2\pi)^3 f(\vec{J})$. With angle-action variables, the Hamiltonian depends only on the momenta, $H = H(\vec{J})$,

and the angle-coordinates increase linearly with time $\vec{\theta} = \vec{\Omega}t + \text{const}$, where $\vec{\Omega} = \partial H / \partial \vec{J}$. The dynamics is thereby reduced to that of “free particles”.

In the action-based DF-fitting method developed by McMillan & Binney (2012, 2013) and further applied and improved by e.g. Ting et al. (2013); Trick et al. (2016); Hattori et al. (2021), the tracer population is assumed to be in equilibrium, and characterized by a DF $f(\vec{J})$. The MW potential is constrained by fitting functional forms for both the total potential and the tracer DF. If the potential is the only function of interest, one further marginalizes over the DF parameters. For instance, Hattori et al. (2021) adopt a model with 9 parameters for the potential and 7 parameters for the DF which are later marginalized over, similarly to other works employing this technique. A disadvantage of this method is that it assumes an analytic expression for the DF, which in reality is unknown.

The main goal of the current paper is to improve on this aspect, by not assuming any functional form for the DF. This avoids the overhead of fitting the DF parameters and possible biases introduced by the chosen DF. Information on the DF is obtained through a non-parametric entropy estimate.

We assume a tracer sample in equilibrium, and described by an unknown DF $f(\vec{r}, \vec{v})$. As for any DF, we can define the so-called differential entropy as

$$S \equiv - \int f \ln f \, d^6 \vec{w}, \quad (1)$$

where $\vec{w} = (\vec{r}, \vec{v})$. This entropy is invariant for changes of variables, and it is thus the same if we change to angle-action variables evaluated in any potential. In the correct potential where the sample is in equilibrium, the DF $f(\vec{r}, \vec{v}) = f(\vec{\theta}, \vec{J})$ is uniform in $\vec{\theta}$. The entropy associated with the angle-variables is then maximum, and to keep S invariant, the entropy associated with the actions must be minimum. This can be easily shown if $f(\vec{\theta}, \vec{J}) = \mathcal{F}(\vec{\theta})F(\vec{J})$, i.e. when the DF is separable, in which case the entropy is just the sum of the entropies in action and angle spaces – in particular, for the fully phase-mixed sample $\mathcal{F}(\vec{\theta}) = (2\pi)^{-3}$. In the Appendix, with the help of conditional expectations, we show that this idea also applies to non-separable DFs.

We explore this idea by using the 6D coordinates of a sample assumed to be in equilibrium and calculating actions in several trial potentials. We then estimate the entropy in action space, with no need to specify a pdf, and accept as the true potential the one with minimum entropy. Although the reasoning above was based on actions, we demonstrate that the same method can be applied to any sets of integrals of motion, provided they respect the symmetry requirements of the problem – e.g.

¹ Although the same concept in practice, we reserve the term DF and the notation $f()$ to the probability density function in 6D, and the term pdf and notation $F()$ to probability density functions in the space of any integrals of motion.

anisotropic spherical systems cannot be simply modeled by $f(E)$, but can be modeled by $f(E, L)$, or by $f(\vec{J})$.

Our approach is thus related to the minimum-entropy estimates of semi-parametric models (Wolsztynski et al. 2005), where the potential is the parametric part and the pdf is the non-parametric one. In Sec. 2 we describe the general formalism, starting from the action-based DF-fitting method and showing how it is extended by our method. Sec. 3 presents the expressions for the entropy estimator in the assumption-free (6D) case and in cases where the DF is a (unknown) function of integrals of motion. Sec. 4 shows the physical basis of the method, investigates the bias and variance of the entropy estimates in different spaces of integrals of motion, and apply a bias correction. In Sec. 5 we use a fixed sample that is phase-mixed in a given potential to illustrate that the entropy of the sample in the space of integrals of motion, calculated in different potentials, is minimum at the true potential. In Sec. 6 we demonstrate through actual fits that our method recovers the true parameters of a simple spherical potential, and of a flattened axisymmetric potential. We discuss our results in Sec. 7 and summarize in Sec. 8.

2. GENERAL FORMALISM

In the DF-fitting method, where an analytical function is assumed for $f(\vec{J})$, one starts defining the likelihood for a star to have coordinates $\vec{w}_i \equiv (\vec{r}_i, \vec{v}_i)$ in a survey volume \mathcal{V} :

$$\mathcal{L}_i(\vec{w}_i|\vec{p}) = \frac{1}{A_i} f(\vec{w}_i|\vec{p}) \mathbb{S}(\vec{r}_i), \quad (2)$$

where $A_i = \int_{\mathcal{V}} f(\vec{w}_i|\vec{p}) \mathbb{S}(\vec{r}_i) d^6 \vec{w}_i$ is a normalization factor taking into account the survey footprint and selection function $\mathbb{S}(\vec{r}_i)$, and $f(\vec{w}_i|\vec{p})$ is the tracer population's DF. In this context, the parameters \vec{p} to be optimized describe the potential and the DF. For simplicity, in these expressions we are not taking into account observational errors, but they can be incorporated – see e.g. McMillan & Binney (2013); Hattori et al. (2021).

The sample joint likelihood is $\mathcal{L} = \prod_{i=1}^N \mathcal{L}_i$, and the log-likelihood to be maximized is

$$\ln \mathcal{L}(\vec{w}|\vec{p}) = \sum_{i=1}^N \ln f_i + \sum_{i=1}^N \ln \left[\frac{\mathbb{S}(\vec{r}_i)}{A_i} \right], \quad (3)$$

where $f_i = f(\vec{w}_i|\vec{p})$. One assumes the tracer population is in equilibrium and described by a DF $f(\vec{J}|\vec{p})$, with the trial potentials entering the fit through the actions.

The formalism above is developed in the context of the DF-fitting method where an analytic DF is assumed. From now on, we shift to the minimum-entropy method

presented here, and in the remainder of this work \vec{p} encapsulates only parameters for the potential. From the Monte Carlo principle, the differential entropy, Eq. (1), can be estimated using a sample of f as

$$\hat{S} = -\frac{1}{N} \sum_{i=1}^N \ln \hat{f}_i, \quad (4)$$

where \hat{f}_i is an estimate² of $f(\vec{w}_i|\vec{p})$, as detailed in Sec. 3. Comparison of Eqs. (3) and (4) suggests defining

$$\ln \lambda(\vec{p}) \equiv -N \hat{S}(\vec{p}) + \sum_{i=1}^N \ln \left[\frac{\mathbb{S}(\vec{r}_i)}{A_i} \right]. \quad (5)$$

Despite appearances, $\ln \lambda(\vec{p})$ is not a log-likelihood for two reasons. First, the expectation value of Eq. (3), $\langle \ln \mathcal{L} \rangle$, does not involve Eq. (1), but

$$\langle \ln \mathcal{L} \rangle = -NH(f_0, f) + N \int f_0 \ln \left(\frac{\mathbb{S}(\vec{r})}{A(\vec{w})} \right) d\vec{w}, \quad (6)$$

where

$$H(f_0, f) = - \int f_0 \ln f d\vec{w} \quad (7)$$

is the cross-entropy, \vec{p}_0 are the *true* parameters and $f_0 = f(\vec{w}|\vec{p}_0)$. Note that $H(f_0, f)$ is minimum for $f = f_0$, illustrating that the maximum likelihood happens at the true parameters (e.g. Akaike 1992). Thus, Eqs. (3) and (5) are only equivalent at the best fit model, i.e. $\ln \lambda(\vec{p}_0) \sim \ln \mathcal{L}(\vec{p}_0)$. Second, $\ln \lambda$ is not a smooth function of the parameters \vec{p} as required by its interpretation as a log-likelihood, but it is noisy since it is based on entropy estimates, rather than the actual entropy. However, as we demonstrate in practice in Sec. 6, and on mathematical grounds in the Appendix, on average $\ln \lambda$ has its maximum at \vec{p}_0 , and can be maximized to find the best fit model – see Fig. 1 for an illustration.

In summary, the maximum-likelihood principle can be replaced by a minimum-entropy one. As illustrated in Fig. 1, fluctuations in $\ln \lambda$ can lead to misidentifying the best fit model, and some smoothing is required to avoid that. In this paper, we estimate the entropy with the k^{th} -Nearest-Neighbor method (kNN, Leonenko et al. 2008), and we smooth out $\ln \lambda$ by averaging over several realizations of the data and by taking $k > 1$ – see Sec. 4.3. After identifying the best fit model by maximizing $\ln \lambda$, we perform an Approximate Bayesian Computation to sample the posterior and get confidence intervals for the parameters, as described in Sec. 6.

Having presented the general formalism, we now show explicit expressions to estimate the entropy in general,

² For any quantity X we denote its estimate by \hat{X} .

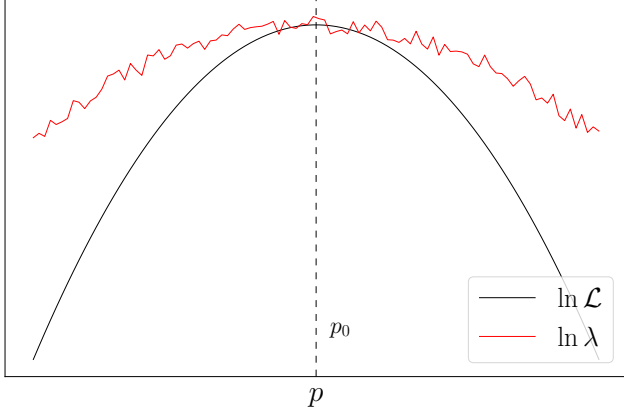


Figure 1. Illustrative scheme comparing the log-likelihood $\ln \mathcal{L}$ with the quantity used to find its maximum, $\ln \lambda$. Although being different quantities, on average they both peak at the same value p_0 and have the same value at the peak.

as well as in particular cases of DFs that are functions of integrals of motion only.

3. ENTROPY ESTIMATORS

We start defining the entropy of a DF $f(\vec{w})$. Instead of Eq. (1), a better formal definition is

$$S \equiv - \int f \ln \left(\frac{f}{\mu} \right) d^6 \vec{w}, \quad (8)$$

where μ is introduced to make the argument in $\ln(f/\mu)$ dimensionless. If $[f] = \text{length}^{-3} \text{velocity}^{-3}$, it is convenient to use coordinates normalized by their dispersions $\sigma_{w_1}, \dots, \sigma_{w_6}$, defining $w'_1 = w_1/\sigma_{w_1}, \dots, w'_6 = w_6/\sigma_{w_6}$. In this case, $\mu = |\Sigma|^{-1}$, where $|\Sigma| = \sigma_{w_1} \dots \sigma_{w_6}$, and with $f'(\vec{w}') = |\Sigma|f(\vec{w})$:

$$S = - \int f' \ln f' d^6 \vec{w}' = - \int f \ln(|\Sigma|f) d^6 \vec{w}. \quad (9)$$

Eq. (9) is the invariant entropy we start from, and from which we transform coordinates for the cases where the DF is a function of integrals of motion only. For a sample of N points, it can be estimated as

$$\hat{S} = - \frac{1}{N} \sum_{i=1}^N \ln \hat{f}'_i, \quad (10)$$

where \hat{f}'_i is an estimate of $f'(\vec{w}'_i)$, and several density estimators can be employed – see Silverman (1986). However, to estimate the entropy with Eq. (10), a few estimators are optimal (Beirlant et al. 1997; Leonenko et al. 2008) – see Beraldo e Silva et al. (2017) for a comparison of different methods in N -body simulations. In this work, we use the k -Nearest Neighbor estimator, where

$$\hat{f}'_i = \frac{1}{(N-1)e^{-\psi(k)}V_d D_{ik}^d}, \quad (11)$$

and

$$V_d = \pi^{d/2}/\Gamma(d/2+1) \quad (12)$$

is the volume of the d -dimensional unit-radius hypersphere, $D_{ik} = \sqrt{(\vec{r}'_i - \vec{r}'_k)^2 + (\vec{v}'_i - \vec{v}'_k)^2}$ is the Euclidean phase-space distance of particle i to its k^{th} neighbor, and $\psi(x)$ is the digamma function³.

For two general distributions f_0 and f , we also re-define their cross-entropy as

$$H(f_0, f) \equiv - \int f_0 \ln \left(\frac{f}{\mu} \right) d^6 \vec{w}. \quad (13)$$

Note that, in general, it is possible to estimate $H(f_0, f)$ even if the samples of f_0 and f have different sizes N and M , respectively. Eq. (13) is estimated as

$$\hat{H} = - \frac{1}{N} \sum_{i=1}^N \ln \hat{\xi}'_i, \quad (14)$$

where

$$\hat{\xi}'_i = \frac{1}{M e^{-\psi(k)} V_d D_{ik}^d}, \quad (15)$$

and now D_{ik} is the distance between point i of the f_0 -sample to its k -nearest neighbor *in the f -sample* (Leonenko et al. 2008). We can interpret $\hat{\xi}'_i$ as an estimate of f at the point i of the f_0 -sample. In this paper, we restrict to samples of equal sizes, so $M = N$. As explained in 6.1, when exploring the posterior distribution of the parameters, f_0 will describe the best fit model obtained in a previous step, and f will describe each trial model.

Eqs. (10) and (14), with Eqs. (11) and (15) respectively plugged in, converge in probability to the true entropies, under weak conditions on the underlying DFs (e.g. Leonenko et al. 2008; Biau & Devroye 2015; Lombardi & Pant 2016). The k -nearest neighbors identification is also fast since it can be optimized with KD-trees.

As explained in the Introduction, the method developed here assumes the sample is in equilibrium in a given potential. In the next subsections, we show explicit expressions for particular cases where the DF only depends on integrals of motion, as required by the Jeans theorem for systems in equilibrium.

3.1. Isotropic spherical system, $f = f(E)$

For isotropic spherical systems in equilibrium, we can write $f(\vec{w}) = f(E)$, where $E = v^2/2 + \phi(r)$ and $\phi(r)$ is the potential. In this case, Eq. (9) reduces to

$$S_E = - \int F(E) \ln \left[\frac{|\Sigma|F(E)}{g(E)} \right] dE, \quad (16)$$

³ In particular, $\psi(1) = -\gamma \approx -0.57722$ (Euler-Mascheroni constant) and, for large k : $\psi(k) \approx \ln(k-1/2) \rightarrow \hat{f}'_i \approx k/(NV_d D_{ik}^d)$.

where

$$F(E) = f(E)g(E) \quad (17)$$

is the pdf in energy space and

$$g[E|\phi(r)] = (4\pi)^2 \int_0^{r_m(E)} r^2 \sqrt{2[E - \phi(r)]} dr \quad (18)$$

is the density of states, with $r_m(E)$ being the radius where $\phi = E$. If σ_E is a typical energy dispersion, we define normalized energies $E' = E/\sigma_E$, and estimate S_E , Eq. (16), as

$$\hat{S}_E = -\frac{1}{N} \sum_{i=1}^N \ln \left[\frac{\hat{F}'_i(E'_i)}{\mu(E_i)} \right], \quad (19)$$

where $\mu(E) = \sigma_E |\Sigma|^{-1} g[E|\phi(r)]$. The pdf in the energy space, $\hat{F}'_i(E'_i)$, is estimated with Eq. (11), with $d = 1$ and $D_{ik} = |E'_i - E'_k|$. If we want to write the density of states in terms of E' , we can make $g[E|\phi(r)] = \sqrt{\sigma_E} g[E'|\phi(r)/\sigma_E]$.

3.2. Anisotropic spherical system, $f = f(E, L)$

For anisotropic spherical systems with a DF $f(\vec{w}) = f(E, L)$, where $L = v_t r$ and $v_t^2 = v_\theta^2 + v_\varphi^2$ in spherical coordinates (r, θ, φ) , Eq. (9) reduces to

$$S_{EL} = - \int F(E, L) \ln \left[\frac{|\Sigma| F(E, L)}{g(E, L)} \right] dE dL, \quad (20)$$

where the pdf for energy and angular momentum is

$$F(E, L) = f(E, L)g(E, L), \quad (21)$$

and

$$g[E, L|\phi(r)] = 8\pi^2 L T_r [E, L|\phi(r)]. \quad (22)$$

The period of radial motion $T_r [E, L|\phi(r)]$ is given by

$$T_r [E, L|\phi(r)] = 2 \int_{r_{\text{per}}}^{r_{\text{apo}}} \frac{dr}{\sqrt{2[E - \phi(r)] - L^2/r^2}}, \quad (23)$$

with r_{per} and r_{apo} being the peri- and apo-center distances. Normalizing the energy and angular momentum as $(E', L') = (E/\sigma_E, L/\sigma_L)$, we estimate S_{EL} as

$$\hat{S}_{EL} = -\frac{1}{N} \sum_{i=1}^N \ln \left[\frac{\hat{F}'_i(E'_i, L'_i)}{\mu(E_i, L_i)} \right], \quad (24)$$

where $\mu(E, L) = \sigma_E \sigma_L |\Sigma|^{-1} g[E, L|\phi(r)]$, and for the pdf we plug in Eq. (11) with $d = 2$ and $D_{ik} = \sqrt{(E'_i - E'_k)^2 + (L'_i - L'_k)^2}$. If one wants to write the density of states in terms of (E', L') , we can replace $g[E, L|\phi(r)] = (\sigma_L^2/\sigma_E) g[E', L'|\phi(r')/(\sigma_L \sqrt{\sigma_E})]$, where $r' = (\sqrt{\sigma_E}/\sigma_L)r$.

3.3. Generic integrable potential, $f = f(\vec{J})$

For realistic galactic potentials, assuming that most orbits are regular or weakly chaotic, we may compute approximate actions with e.g. the Stäckel approximation (Binney 2012). In this context, a system in dynamical equilibrium is described by a pdf in action space

$$F(\vec{J}) = (2\pi)^3 f(\vec{J}), \quad (25)$$

where \vec{J} are three actions. Thus, Eq. (9) reduces to

$$S_{\vec{J}} = - \int F(\vec{J}) \ln \left[\frac{|\Sigma| F(\vec{J})}{(2\pi)^3} \right] d\vec{J}. \quad (26)$$

The simplicity of Eq. (26), in comparison to Eqs. (16)-(18) or Eqs. (20)-(23), illustrates the advantages of using action-based DFs instead of other integrals of motion. Defining new actions \vec{J}' normalized by their dispersions $(\sigma_{J_1}, \sigma_{J_2}, \sigma_{J_3})$, we have

$$\hat{S}_{\vec{J}} = -\frac{1}{N} \sum_{i=1}^N \ln \left[\frac{\hat{F}'_i(\vec{J}'_i)}{\mu} \right], \quad (27)$$

where $\mu = (2\pi)^3 \sigma_{J_1} \sigma_{J_2} \sigma_{J_3} |\Sigma|^{-1}$, and for the pdf we plug in Eq. (11) with $d = 3$ and $D_{ik} = \sqrt{|\vec{J}'_i - \vec{J}'_k|^2}$.

The same expressions apply to the cross-entropy estimates, Eqs. (14)-(15), *mutatis mutandis*.

Having presented the expressions in general and for DFs depending only on integrals of motion, in the next section we illustrate the physical basis of the method, as well as investigate the bias and fluctuation in these estimates. For that, we use a model with explicit expressions for $f(E)$, $g(E)$ and for the actions.

4. THE ISOCHRONE MODEL

To illustrate the accuracy of these entropy estimators and the physical basis of our method, we start generating a self-consistent sample of the Isochrone model (Hénon 1959), whose potential is

$$\phi(r) = -\frac{GM}{b} \frac{1}{1 + \sqrt{1 + (r/b)^2}}, \quad (28)$$

where M is the total mass and b the scale length. The DF of a self-consistent sample is (see Binney & Tremaine 2008; Binney & Petrou 1985)

$$f(E) = \frac{1}{\sqrt{2}(2\pi)^3 (GMb)^{3/2}} \frac{\sqrt{\varepsilon}}{[2(1 - \varepsilon)]^4} \times \left[27 - 66\varepsilon + 320\varepsilon^2 - 240\varepsilon^3 + 64\varepsilon^4 + 3(16\varepsilon^2 + 28\varepsilon - 9) \frac{\sin^{-1} \sqrt{\varepsilon}}{\sqrt{\varepsilon(1 - \varepsilon)}} \right], \quad (29)$$

and the density of states, Eq. (18), is

$$g(E) = (2\pi)^3 \sqrt{GMb}^{5/2} \frac{(1-2\varepsilon)^2}{(2\varepsilon)^{5/2}}, \quad (30)$$

where $\varepsilon = -bE/(GM)$. The radial period is

$$T_r(E, L) = \frac{2\pi GM}{(-2E)^{3/2}}. \quad (31)$$

As for any spherical system, the azimuthal and latitudinal actions are $J_\varphi = L_z$ and $J_\theta = L - |L_z|$, respectively, and the radial action is

$$J_r = \frac{1}{\pi} \int_{r_{\text{per}}}^{r_{\text{apo}}} dr \sqrt{2E - 2\phi(r) - \frac{L^2}{r^2}}. \quad (32)$$

For the Isochrone potential,

$$J_r = \frac{GM}{\sqrt{-2E}} - \frac{1}{2} \left(L + \sqrt{L^2 + 4GMb} \right). \quad (33)$$

4.1. Entropy bias

Setting $G = M = b = 1$, we start evaluating the integral in Eq. (16) numerically, from $E_{\text{min}} = -0.5$ to $E_{\text{max}} = -10^{-8}$, using Eqs. (29)-(30). We take this as the true entropy value, shown as a thick solid gray line in Fig. 2 (upper panel). Then, we generate samples of this model with different sizes N using AGAMA (Vasiliev 2019), and integrate orbits for these samples in the self-consistent potential for $50 \times \langle T_{\text{circ}} \rangle$, where T_{circ} is the period of circular motion. We estimate the entropy of the sample S_{6D} , Eq. (9), with Eqs. (10)-(12) at different times, taking the nearest neighbor ($k = 1$). We recalculate $|\Sigma| = \sigma_{w_1} \dots \sigma_{w_6}$, renormalizing the coordinates at each time. This provides better estimates than using a fixed initial normalization, but the difference is small. This is shown as thin solid lines for different numbers of particles in Fig. 2, upper panel.

Since the initial sample is self-consistent with the potential, it is stationary and \hat{S}_{6D} should be conserved. We see that this is the case for all sample sizes, with larger fluctuations for smaller N . Furthermore, \hat{S}_{6D} is significantly biased in respect to the true value, and this bias is time-independent. In the bottom panel, the hexagons show the relative bias $\delta S_{6D} = (\langle \hat{S}_{6D} \rangle_t - S_{\text{true}}) / S_{\text{true}}$ as a function of N , where $\langle \hat{S}_{6D} \rangle_t$ is a time-average. Even for $N = 10^8$, \hat{S}_{6D} has a relative bias of $\approx 1.5\%$.

The dashed colored lines in the upper panel show the entropy estimated in the action space, $S_{\mathcal{J}}$, using Eq. (27), i.e. assuming the DF is an unknown function of the actions. Since these are conserved, we only estimate $S_{\mathcal{J}}$ at $t = 0$. We see that $\hat{S}_{\mathcal{J}}$ produces a much smaller bias with respect to the true value, due to the dimension reduction from 6D to 3D. The triangles in the

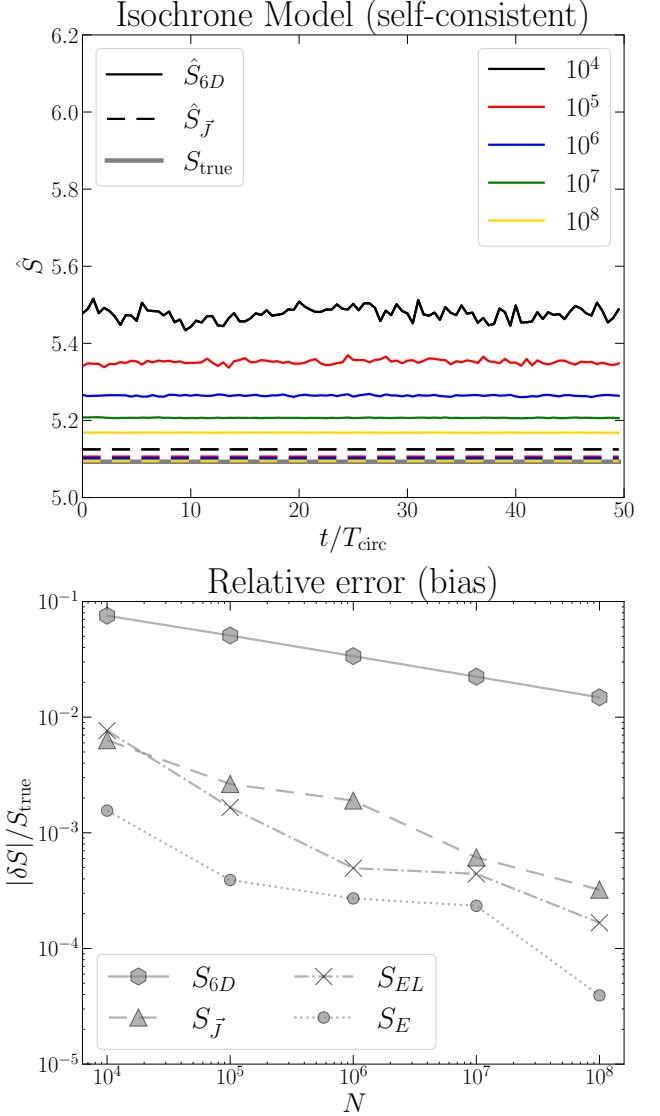


Figure 2. Upper panel: entropy estimates in 6D (solid) and in action space (dashed) for self-consistent samples of the Isochrone model, with different sample sizes (colors). The thick solid gray line shows the true value – numerical integral in Eq. (16). Bottom panel: relative error (bias) of \hat{S}_{6D} , $\hat{S}_{\mathcal{J}}$, \hat{S}_{EL} and \hat{S}_E . For a fixed sample size, estimates in lower dimensions are more precise.

bottom panel show that the bias stays below $\approx 1\%$ even for $N = 10^4$. The dots and crosses show the relative bias for \hat{S}_E and \hat{S}_{EL} , respectively. These are estimated with Eq. (19) for S_E , i.e. assuming the DF is an unknown function $f = f(E)$, and Eq. (24) for $S_{E,L}$. We see that the bias is also significantly smaller than that of \hat{S}_{6D} .

Thus, we have shown that: \hat{S}_{6D} is appropriately conserved in the self-consistent model, but it is biased with respect to the true value by $\delta S/S_{\text{true}} \approx 7.5\%$ for $N = 10^4$; and in the space of integrals of motion the

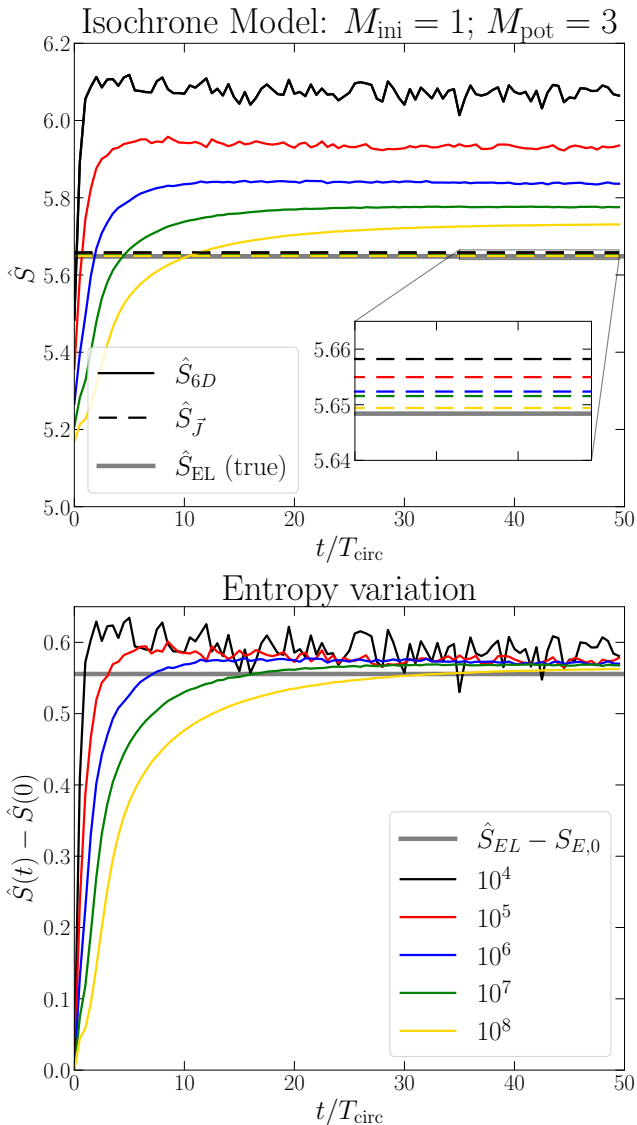


Figure 3. Upper panel: entropy estimates in 6D (solid) and in action space (dashed) for initial self-consistent samples of the Isochrone model with $M = 1$, but integrated in an Isochrone potential with $M = 3$. The thick solid gray line shows the entropy for a phase-mixed system with $f = f(E, L)$ and $N = 10^8$, considered as the true final entropy. Bottom panel: entropy variation $\Delta\hat{S} = \hat{S}(t) - \hat{S}(0)$ for different sample sizes, which approximately converges to the true ΔS for all samples.

estimates recover the true entropy with $\delta S/S_{\text{true}} \lesssim 1\%$ for $N = 10^4$, and $\delta S/S_{\text{true}} \approx 0.01\%$ for $N = 10^8$.

Next we use the same initial samples but calculate the energies and actions in a new Isochrone potential with $M = 3$ and $b = 1$. We integrate orbits for these samples in the new potential for $50 \times \langle T_{\text{circ}} \rangle$, which is enough for the sample to relax (phase-mix), and estimate the entropy at several time-steps. In Fig. 3 upper

panel, solid (dashed) lines represent \hat{S}_{6D} ($\hat{S}_{\mathcal{J}}$). Since the initial sample is far from stationary in the new potential, it responds to the higher mass developing a radially biased velocity anisotropy. The final DF is unknown, but it should respect the Jeans theorem, being a function $f(E, L)$. The thick solid gray line shows \hat{S}_{EL} for $N = 10^8$ in the new potential, which is the lower dimension allowed by the phase-mixed sample. Since we have shown that \hat{S}_{EL} has a negligible bias for $N = 10^8$, we take this as the true final entropy.

Besides the biases with respect to the initial true entropy $S_{E,0}$ (see Fig. 2), Fig. 3 shows that the asymptotic values of \hat{S}_{6D} ($t \rightarrow \infty$) in the new potential are also biased with respect to the true final value \hat{S}_{EL} . On the other hand, $\hat{S}_{\mathcal{J}}$ is again much less biased. In both cases the bias decreases for larger N – see the inset plot.

The bottom panel shows $\Delta\hat{S}_{6D} = \hat{S}_{6D}(t) - \hat{S}_{6D}(0)$ (colored) and the true entropy increase $\Delta S_{EL} = \hat{S}_{EL} - S_{E,0}$ (thick gray). The final $\Delta\hat{S}_{6D}$ is similar for all sample sizes and it approximately converges to the true ΔS_{EL} . This confirms that the bias is nearly independent of time and is thus nearly eliminated by calculating entropy variations, as done by Beraldo e Silva et al. (2017, 2019b,a).

We also note that a larger N delays the entropy increase, and the entropy would be conserved in the limit $N \rightarrow \infty$. This agrees with the prediction of the Vlasov equation, $df/dt = 0$, which is based on this limit – see Beraldo e Silva et al. (2019b,a). However, in this case the system would never achieve a stationary state described by the Jeans theorem. In other words, in order for the system to respect the Jeans theorem at some time, the continuum phase-space assumption ($N \rightarrow \infty$, and with it the Vlasov equation) must be invalid before, even for perfectly collisionless systems such as the ones considered here – we further discuss this in Sec. 7.

If the bias of \hat{S} is the same for all models, i.e. independent of the parameters, it poses no problem for the minimum-entropy fits, since it only introduces an additive constant in \hat{S} . Our results suggest that the bias may depend weakly on the parameters, thus introducing a bias in the fits. We next investigate this bias in more detail and test a prescription to suppress it.

4.2. Bias correction

It is well known that taking the k^{th} neighbor for larger k increases the bias in the entropy estimate, but decreases its variance, a manifestation of the common bias-variance trade-off in statistical analysis. To investigate this, we generate 10^3 different realizations of size- N samples of the Isochrone model with $M = b = 1$. Then we calculate actions and $\hat{S}_{\mathcal{J}}$, Eq. (27), in the self-consistent

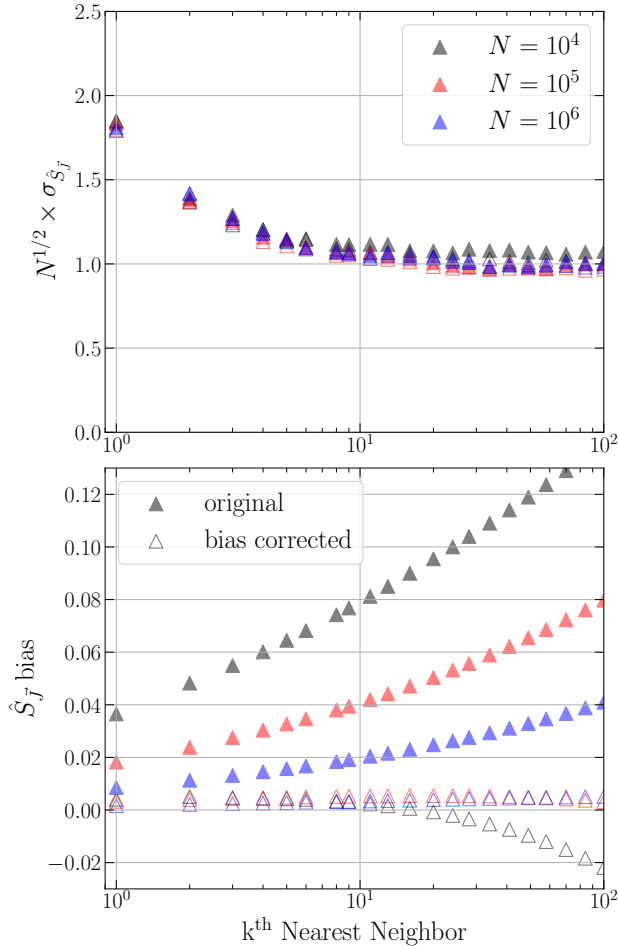


Figure 4. Top: the fluctuation $\sigma_{\hat{S}_j}$, for a self-consistent Isochrone sample, selecting the k^{th} neighbor. It decreases with k , saturating at $\sigma_{\hat{S}_j} \approx 1/\sqrt{N}$ for $k \approx 10$. Bottom: the bias in \hat{S}_j , confirming it increases with k . Full (empty) triangles are for the estimates without (with) the bias correction. Empty blue and red triangles nearly overlap.

potential for each of these realizations, normalizing the actions in each one. Since in this case we are not comparing with \hat{S}_{6D} , we do not normalize physical coordinates by $|\Sigma|$, which would introduce unnecessary extra noise.

The full triangles in Fig. 4 (bottom panel) show the bias (the difference between the mean of the realizations and the true value) as a function of k for different sample sizes. We confirm the increase in the bias for larger k . Taking $k = 10$ introduces a bias which is ~ 2 times larger than that of $k = 1$.

We investigate the correction for the bias proposed by Charzyńska & Gambin (2015). The idea is that the bias is essentially due to points near the edges of the distribution support. For these points, the hyper-sphere around the point (defined by the distance to the neighbor) can have a fraction of its volume outside the support. Since

this results in overestimating the volume, Eq. (11) ends up underestimating the DF for these points. When plugged into Eq. (10), this will produce a positive bias, in accordance with our results – see Figs. 2–4. To compensate for this, Charzyńska & Gambin (2015) propose to add the following correction to the entropy estimate:

$$C = \frac{1}{N} \sum_{i=1}^N \ln \left(\frac{|v(\vec{w}_i, D_{ik}) \cap \text{supp}(W)|}{|v(\vec{w}_i, D_{ik})|} \right), \quad (34)$$

where D_{ik} is the distance to the k -nearest neighbor and $v(\vec{w}_i, D_{ik})$ is the volume around point \vec{w}_i , which is drawn from W , in d -dimensions.

Since it is hard to determine the shape of the support and to appropriately calculate the intersections in Eq. (34) in general, Charzyńska & Gambin (2015) propose to assume a hyper-rectangular box for the support and a hyper-cubic box for the volume $v(\vec{w}_i, D_{ik})$, although their analysis restricts to $k = 1$. Assuming cubic boxes of side l_i , we identify points with $w_{j,i} > w_{j,\max} - l_i/2$, or $w_{j,i} < w_{j,\min} + l_i/2$, where $j = 1, \dots, d$, and calculate the volume fractions of the cube inside the rectangular box. Concisely, it results that

$$C = \frac{1}{N} \sum_{i=1}^N \sum_{j=1}^d \ln \left[\frac{\min\left(\frac{w_{j,\max}}{l_i}, \frac{w_{j,i}}{l_i} + \frac{1}{2}\right) - \max\left(\frac{w_{j,\min}}{l_i}, \frac{w_{j,i}}{l_i} - \frac{1}{2}\right)}{1} \right]. \quad (35)$$

After a few experiments, we chose to use the cube inscribed to the sphere of radius D_{ik} , i.e. $l_i = (2/\sqrt{d})D_{ik}$. The empty triangles in Fig. 4 (bottom panel) show the corrected biases, which are smaller than in the original estimates by factors 5 – 15 – note that the empty blue and red triangles nearly overlap. The improvement is even better when we consider larger k , for which the bias is not larger than that for $k = 1$ (up to a certain k , beyond which the bias is over-corrected).

4.3. Entropy fluctuation

As mentioned in Sec. 2, the random noise in the entropy estimates is one of the reasons why $\ln \lambda$, Eq. (5), is not a log-likelihood. On theoretical grounds this noise is expected to be $\sigma_{\hat{S}} \approx N^{-1/2}$ (Biau & Devroye 2015). The top panel of Fig. 4 shows the entropy fluctuation $\sigma_{\hat{S}_j}$ as a function of k . This fluctuation is estimated as half the 16 – 84th-inter-percentile range of the realizations, and is multiplied by $N^{1/2}$. We confirm the expected trend of $\sigma_{\hat{S}} \approx N^{-1/2}$, and we see that $\sigma_{\hat{S}}$ decreases with k , but it saturates at $k \approx 10$, reducing $\sigma_{\hat{S}_j}$ by a factor ≈ 2 in comparison to $k = 1$. Empty triangles show the fluctuations for the bias-corrected estimates, and we see that the correction does not introduce extra noise.

In summary, we conclude that taking $k = 10$ for a sample of size $N = 10^4$ suppresses the random noise by a factor 2, and the bias correction proposed by Charzyńska & Gambin (2015) does not increase the noise.

5. MINIMUM ENTROPY ILLUSTRATED

In the Appendix, we show on mathematical grounds why the entropy estimates should be minimum in the correct potential, i.e. in the one where the sample is phase-mixed. In this section, we illustrate this with phase-mixed samples in several different models. We generate an initial sample of the Isochrone model with $M = b = 1$, and sample size $N/0.7$, selecting the 70% most bound particles in the self-consistent potential, with a final sample of $N \approx 10^4$. This selection allows us to explore a larger set of models, since we restrict to models where all particles are bound. Note that this cut does not affect the method because the DF is still a function of integrals of motion only, and self-consistency is not required as we explicitly demonstrate below.

We calculate the entropy in action space in a grid of parameter values (M, b) . We consider an ideal, error-free, sample of size N in a survey covering the whole sky with selection function $\mathbb{S}(\vec{r}_i) = 1$. Thus, in Eq. (5), $A_i = 1$, and in this case the maximum of $\ln \lambda(\vec{p})$ is strictly equivalent to the minimum-entropy. In this exercise, we do not correct the bias as discussed in Sec. 4.2.

Fig. 5 shows $\hat{S}_{\mathcal{J}}$ values in the grid (M, b) , using the nearest neighbor, $k = 1$ (left), and $k = 10$ (right). The magenta dots show the true parameters, and the white X's show the location of the minimum entropy. The white curves are illustrative contours of the 1st, 5-th and 10-th percentiles of $\hat{S}_{\mathcal{J}}$ (not confidence levels). The minimum entropy is indeed very near the true values. We note, however, that the exact location of this minimum depends on the sample realization. The wrinkles in the colors and contours in the left panel reveal the noise in $\hat{S}_{\mathcal{J}}$ for $k = 1$, while for $k = 10$ the surface is much smoother, in agreement with Fig. 4 (upper panel).

At this point, the reader might think that the correct identification of the potential with the minimum entropy depends on something special about the Isochrone potential, or the fact that we have a self-consistent sample, as opposed to a generic stationary sample. To disperse this concern, we now use the same sample as initial conditions and integrate orbits in four different potentials. For this, we use the hypervirial family of Evans & An (2005), characterized by the potential/density pair

$$\phi(r) = -\frac{GM}{a} \frac{1}{[1 + (r/a)^p]^{1/p}}, \quad (36)$$

$$\rho(r) = \frac{(p+1)M}{4\pi a^3} \frac{(r/a)^{p-2}}{[1 + (r/a)^p]^{2+1/p}}, \quad (37)$$

where $0 < p \leq 2$ for the most physically interesting cases. These models have $\rho \sim r^{p-2}$ near the center and $\rho \sim r^{-(p+3)}$ in the outskirts, and have finite mass M . Their most interesting property is that they respect the virial theorem locally, besides the usual global one. We use these models for their simplicity and because they reduce to well known models for $p = 1$ (Hernquist 1990), and $p = 2$ (Plummer 1911). We also explore the cases $p = 1/2$ (strong cusp) and $p = 3/2$ (weak cusp). We set $G = a = 1$, but set $M = 2$ in order to have only bound orbits in all models. We integrate orbits for $100 \times \langle T_{\text{circ}} \rangle$, which is enough for the samples to phase-mix within each potential. This creates, for each of the four potentials, a different equilibrium (phase-mixed) DF, with no explicit analytic expression. Then, for each of these four phase-mixed samples, we calculate the actions $(J_r, J_\varphi, J_\theta)$ and $\hat{S}_{\mathcal{J}}$ in trials potentials (M, a) .

Fig. 6 shows the entropy surface for these different potentials. We see that the minima (white crosses) lie very close to the true values (magenta dots), but once more their exact locations depend on the particular data realization. This shows that the only requirement to fit the potential by minimizing the entropy is that the sample is stationary, with self-consistency playing no special role. Let us emphasize that this procedure does not require knowledge of the sample's density or anisotropy profile, or its DF, but only assumes that the DF is an unknown function satisfying the Jeans theorem, i.e. $f = f(\vec{J})$.

Fig. 7 shows a similar picture, but with the entropy calculated in the space of energy and angular momentum, using Eqs. (22)-(24), with T_r calculated as $2\pi/\Omega_r$, where Ω_r is the radial frequency calculated with AGAMA. Once more the entropy minima are close to the true values for all models. We also note that this \hat{S}_{EL} is slightly noisier than $\hat{S}_{\mathcal{J}}$, even though the former is defined in 2D and its statistical noise is thus expected to be smaller. We believe that this is related to the support of the remaining variables, i.e. the angles, being independent of the actions, while the use of other integrals leaves remaining variables whose support can depend on the integrals. This issue is discussed in more detail in the Appendix, after Eq. (A6), further illustrating the usefulness of the canonical character of actions.

6. MODEL FITTING

Having demonstrated that $\hat{S}_{\mathcal{J}}$ is minimum at the true parameters of the probed potentials, we now perform actual fits through Eq. (5) to recover the potential where the tracer population is in equilibrium. In Sec. 6.1 we fit the Isochrone potential, and in Sec. 6.2 we fit an axisymmetric flattened potential.

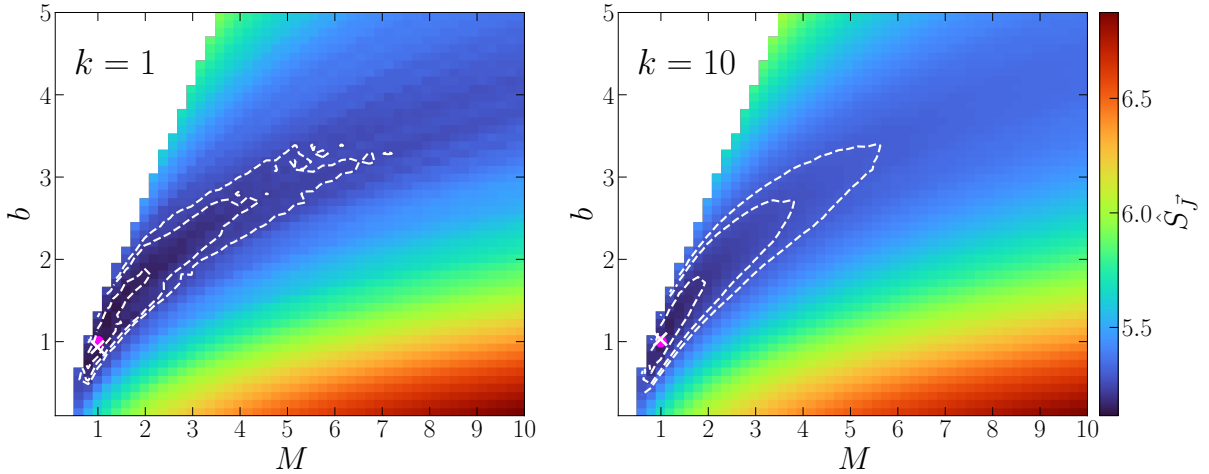
Isochrone potential: $N \approx 10^4$ 

Figure 5. The $\hat{S}_{\mathcal{J}}$ -surface in a grid of parameter values (M, b) of the Isochrone potential, obtained with a self-consistent sample of the model $(M, b) = (1, 1)$ (magenta dots). The white X's show the minima of $\hat{S}_{\mathcal{J}}$. Contours are percentile levels of $\hat{S}_{\mathcal{J}}$. The entropy is estimated with the nearest-neighbor, $k = 1$ (left), and with $k = 10$ (right). We see that the entropy is minimum near the true potential where the sample is phase-mixed. As expected, a larger k smooths out the $\hat{S}_{\mathcal{J}}$ -surface.

6.1. Fitting the Isochrone potential

In order to suppress the noise in the entropy estimates, we generate 100 realizations of a self-consistent sample of the Isochrone Model with $M = b = 1$, and sample size $N/0.7$, selecting the 70% most bound particles in each sample, with final samples of $N \approx 10^4$. Assuming that the DF is an unknown function $f(\vec{J})$, for each trial Isochrone potential we estimate $S_{\mathcal{J}}$, Eq. (27), for each realization, taking the k -th neighbor with $k = 10$ and correcting for the bias as discussed in Sec. 4.3. We finally calculate the mean over realizations $\langle \hat{S}_{\mathcal{J}} \rangle$.

We set $\mathbb{S}(\vec{r}_i) = A_i = 1$ in Eq. (5) for a complete sample in a whole-sky survey, and use the downhill simplex (“Nelder-Mead”), as implemented in `scipy`, to maximize $\ln \lambda(\vec{p}) = -N \langle \hat{S}_{\mathcal{J}} \rangle$, i.e. to minimize the entropy. To prevent trapping at local maxima, we fit the data starting with initial parameters in a regular grid of 10×10 points, with $0.1 < M < 10$, and $0.1 < b < 5$. We fit only those models producing no unbound particle on more than 50% of the realizations and taking the entropy average over those realizations, setting $\ln \lambda = -\infty$ for the remaining models. We select the best fit model as the one with largest $\ln \lambda$ among all fits.

Having found the best fit model, we characterize the model posterior probability to determine uncertainties and correlations of the parameters. Since we do not have a *bona fide* log-likelihood, we cannot use traditional Markov Chain Monte Carlo sampling. Instead, we use simulation-based inference to characterize the posterior (see Cranmer et al. 2020, for a recent review). In par-

ticular, we perform an Approximate Bayesian Computation (ABC – see Beaumont et al. 2002; Sisson et al. 2018; Martin et al. 2021), a sampling-rejection method that allows sampling the posterior in problems where the log-likelihood is unknown or intractable (see Hahn et al. 2017, for an application in cosmology).

In an ABC analysis, one starts sampling models from a prior distribution. For each model, a new dataset is generated (simulated) and compared with the observed data via direct comparison or some summary statistics. In our case, the “observational data” are the actions evaluated in the best fit model. The trial model is then accepted if the distance between the two datasets is smaller than a distance threshold ϵ , and rejected otherwise. Depending on the required precision on the posterior, i.e. depending on ϵ , the original method can be very inefficient, and several different techniques exist to adapt the sampling function and ϵ iteratively. In this work, we use the so-called sequential Monte Carlo (Sisson et al. 2007) as implemented in the python package `pyABC` (Schälte et al. 2022). In this algorithm, the first sampling is made from the prior, and subsequent iterations sample from functions that are better approximations of the posterior at each iteration. This process is driven by an iterative decrease in ϵ , with a consequent decrease in the samples acceptance rate. The process can be considered to converge after the distance threshold or the acceptance rate fall below a certain value, or the changes in the posterior become negligible.

As a distance metrics between the best fit model f_0 and each trial model f , we use the Kullback-Leibler di-

Initial condition: Isochrone sample; $N \approx 10^4$; Action-space

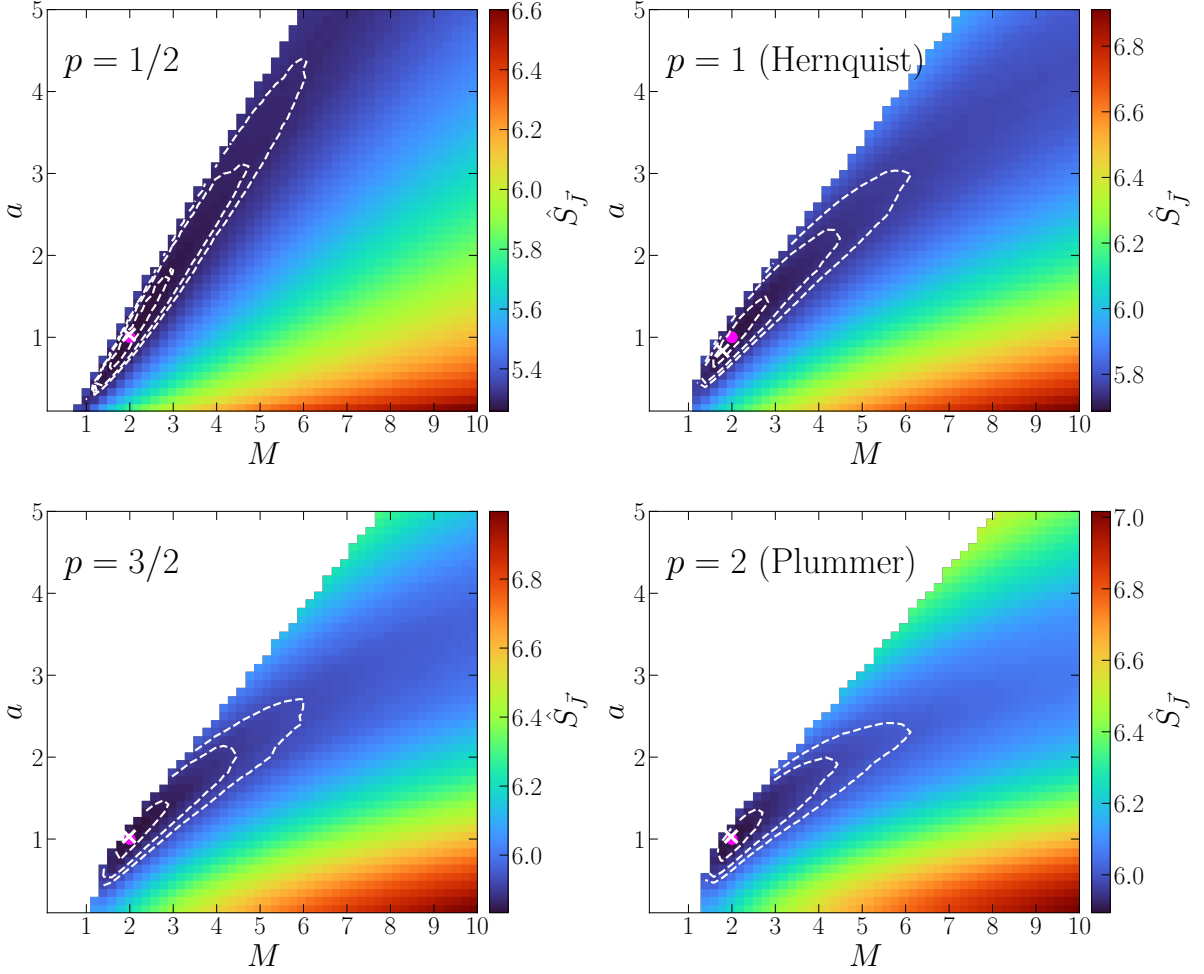


Figure 6. The $\hat{S}_{\vec{J}}$ -surface in a grid of parameters (M, a), calculated in the action-space. Each panel is for a different potential of the hypervirial family of Evans & An (2005), where the same initial sample phase-mixed. Magenta dots show the true values, and the white X, the minimum of $\hat{S}_{\vec{J}}$, with contours showing percentile levels. The entropy is estimated with the $k = 10$ nearest-neighbor. For all models, $\hat{S}_{\vec{J}}$ has its minimum near the correct parameters.

vergence (see e.g. Jiang 2018)

$$D_{\text{KL}}(f_0||f) \equiv \int f_0 \ln \left(\frac{f_0}{f} \right) d\vec{J} = H(f_0, f) - S_0, \quad (38)$$

where $S_0 = \hat{S}_{\vec{J}}(f_0)$. For two distributions f and g in general, $D_{\text{KL}}(f||g)$ can be seen as a directed distance from f to g . In fact, $D_{\text{KL}}(f||f) = 0$, and it can be shown that $D_{\text{KL}}(f||g) \geq 0$ (Kullback 1968). In practice, we compute $D_{\text{KL}}(f_0||f)$ using the estimator for the cross-entropy $H(f_0, f)$ – see Eqs. (13)-(15).

We assume flat priors $0.1 \leq M \leq 5$ and $0.1 \leq a \leq 5$ and run pyABC for several iterations. We require 10^4 models to be accepted in each iteration, and we run pyABC until the acceptance rate falls below 10^{-3} . Thus,

the final iterations are more time consuming since many models are generated until the desired number of models are accepted. ABC requires generating a new data sample for each trial model, otherwise the algorithm converges to point-wise estimates and do not explore the posterior. In order to investigate the ideal situation without observational errors, for each model we generate a different realization of a sample in equilibrium in the best fit model. In practice, when one has a single observed dataset at hand, one can generate new realizations sampling from an assumed error distribution around the observed values, as we do in Sec. 6.2.

Fig. 8 shows the distance threshold ϵ_t and the acceptance rate at each iteration t . After ~ 10 iterations, the

Initial condition: Isochrone sample; $N \approx 10^4$; (E,L)-space

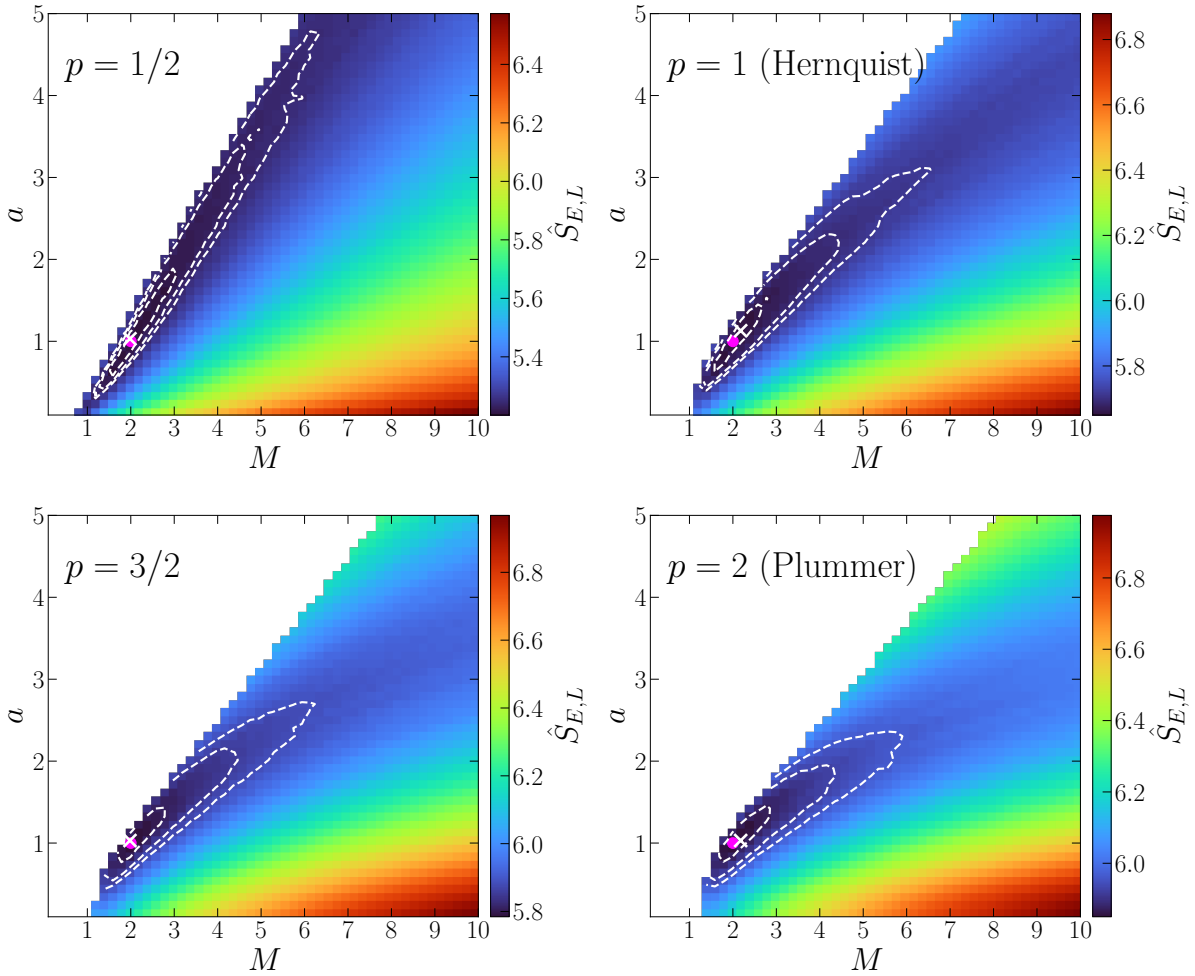


Figure 7. Similar to Fig. 6, but calculated in the (E,L)-space. The minima of $\hat{S}_{E,L}$ (white crosses) again are close to the true values (magenta dots), but the $\hat{S}_{E,L}$ -surface has more wrinkles, revealing a larger noise.

distance threshold evolves mildly, while the acceptance rate keeps decreasing steadily, making the sampling inefficient at higher iterations. Fig. 9 shows the approximated posterior at different iterations, with magenta dots showing the true values. It is clear that the algorithm approximately converges after ~ 10 iterations.

Fig. 10 is a corner plot of the last iteration, with blue lines indicating true values, and red contours representing percentiles 39.3 and 86.4 ($1\text{-}\sigma$ and $2\text{-}\sigma$ equivalent contours in 2D). Dashed lines show the percentiles 16, 50 and 84, illustrating the best fit values and $1\text{-}\sigma$ equivalent regions in the marginal distributions of individual parameters. The true parameters are recovered with $\sim 2\%$ errors, and statistical uncertainties $\sim 10 - 15\%$.

To illustrate the role of the k -th neighbor in the entropy estimate, Fig. 11 shows a corner plot similar to

Fig. 10, but now taking $k = 1$, i.e. the nearest neighbor. In agreement with the analysis of Sec. 4.3, in this case the estimates are noisier, resulting in fits that are less accurate, less precise and having less smooth contours, but the true values are still well recovered.

6.2. Fitting an axisymmetric potential

Having demonstrated the ability of our method to fit simple spherical models, we now use a MW halo-like sample to fit an axisymmetric potential. This potential is a modified version of the DM halo potential of [McMillan \(2017\)](#), where we introduce a flattening parameter q , i.e. the ratio between the minor and major axes. The

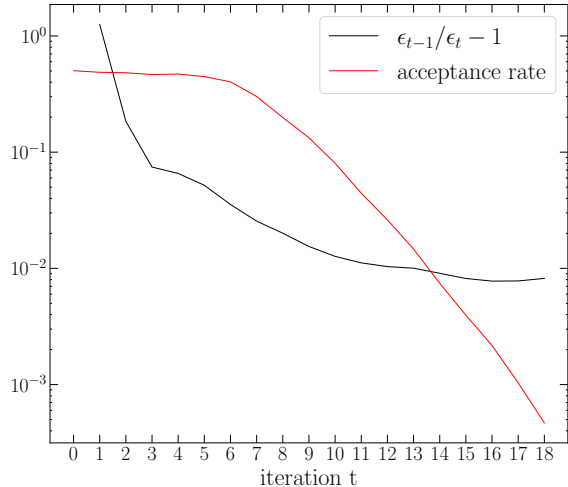


Figure 8. The evolution of the distance threshold ϵ_t and acceptance ratio as a function of the iteration t in the ABC analysis to fit the isochrone potential. In the fit, we estimate the entropy in the action space with the $k = 10$ neighbor.

potential is that associated with the density profile

$$\frac{\rho_{DM}(\tilde{r})}{\rho_0} = \left(\frac{\tilde{r}}{r_s}\right)^{-\gamma} \left[1 + \left(\frac{\tilde{r}}{r_s}\right)\right]^{\gamma-3} \exp\left[-\left(\frac{\tilde{r}}{400\text{kpc}}\right)^6\right], \quad (39)$$

where $\rho_0 = 8.53702 \times 10^6 M_\odot/\text{kpc}^3$, $r_s = 19.5725$ kpc, $\gamma = 1$, $\tilde{r} = \sqrt{x^2 + y^2 + (z/q)^2}$ and $q = 0.7$. The exponential term is just a cutoff to assure a finite mass and to avoid numerical problems. In principle, this DM halo potential could be added to all the other components of the [McMillan \(2017\)](#) potential, even if we only fit the parameters of the former. However, in this case the inner potential would be dominated by the baryonic components and the number of star-particles of our tracer sample (described below) in the outer regions would not be large enough to constrain the DM halo parameters.

We use AGAMA to generate a spherical stellar halo sample of $N = 10^4$ particles (the tracers), with a broken power-law density profile given by

$$\rho_h(r) \propto \left(\frac{r}{r_h}\right)^{-2.5} \left[1 + \left(\frac{r}{r_h}\right)\right]^{-0.5} \exp\left[-\left(\frac{r}{300\text{kpc}}\right)^3\right], \quad (40)$$

where $r_h = 25$ kpc, and the exponential term is again a cutoff at large radii to avoid numerical problems. We set the velocities such that this sample is stationary in our axisymmetric potential. Specifically, we first create a sphericalized version of the potential and initialize the isotropic DF using the Eddington inversion formula, then express this DF as a function of actions, embed it in the flattened potential, and sample both positions and velocities of stars from the resulting system. This

procedure is equivalent to adiabatically deforming the potential from the initial (spherical) to the final (non-spherical) shape. We do not apply any geometric cut or selection function intended to reproduce a realistic survey, and thus we have $\mathbb{S}(\vec{r}_i) = A_i = 1$ in Eqs. (5)-(6).

We use this sample to fit the potential parameters ρ_0 , q , γ , and r_s , assuming that the sample is described by an unknown DF $f(\vec{J})$. We use AGAMA to estimate the actions $\vec{J} = (J_r, J_\varphi, J_z)$ in each trial potential through the Stackel fudge ([Binney 2012](#)). As in [Sec. 6.1](#), we first identify the best fit model maximizing $\ln \lambda$, [Eq. \(5\)](#), starting in a grid of parameter values, and averaging the entropy estimates over 100 sample realizations. We then use the actions in the globally best fit model as the “observed data” in the ABC to characterize the posterior distributions of parameters.

Once more, we run pyABC for several iterations, accepting 10^4 models in each iteration and generating a new data sample (\vec{w}) for each potential. Different from [Sec. 6.1](#), where each new sample was an equilibrium sample of the best fit model, here we generate samples from a Gaussian error distribution centered on the “observed coordinates”, which is similar to what one would do when dealing with observational data. [Fig. 12](#) shows the corner plot obtained assuming 1% uncertainty on all phase-space coordinates (Gaussians of width $\sigma_{w_i}/|w_i| = 0.01$). The algorithm is run until the acceptance rate falls below 10^{-2} , by which time the true parameters are well recovered. This suggests that this acceptance rate is a reasonable choice when dealing with observed data, where the true answer is unknown.

[Fig. 13](#) shows a similar plot, obtained with Gaussian error distributions with $\sigma_{w_i}/|w_i| = 0.2$ for each coordinate, which is more realistic and maybe a little pessimistic. We clearly see the worsening of the fit quality in comparison to [Fig. 12](#), but the true parameters are still recovered reasonably well. In particular, the flattening parameter is recovered with uncertainty $\sim 10\%$.

7. DISCUSSION

7.1. Why does the method work?

It is commonly accepted that the Vlasov equation, $df/dt = 0$, describes the evolution of collisionless systems (i.e. those in smooth potentials) towards a stationary state constrained by the Jeans theorem. That equation, based on the limit $N \rightarrow \infty$ (continuum assumption), predicts indefinitely fine phase-space structures and entropy conservation.

In [Sec. 4](#), we explored self-consistent samples of the Isochrone model, which has analytical expressions for $f(E)$, $g(E)$ and actions. In this case we calculate the true entropy to machine precision, and compare it with

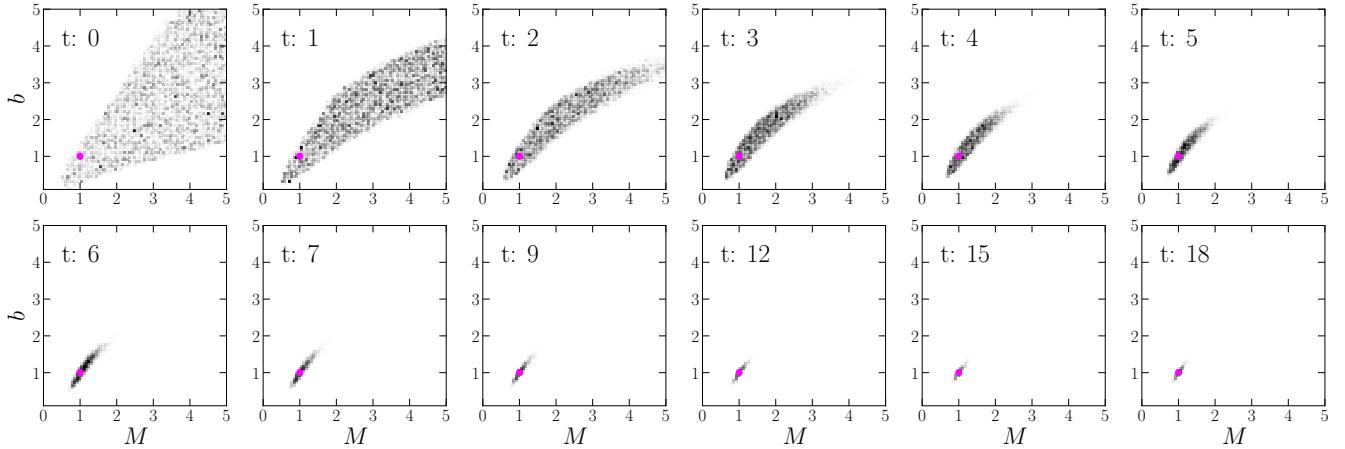


Figure 9. The evolution of the approximated posterior distribution as a function of the iteration t in the ABC analysis to fit the isochrone potential. The true parameters $(M, b) = (1, 1)$ are indicated by magenta dots. We estimate the entropy in the action space with the $k = 10$ neighbor, and correct for the bias as discussed in Sec. 4.2.

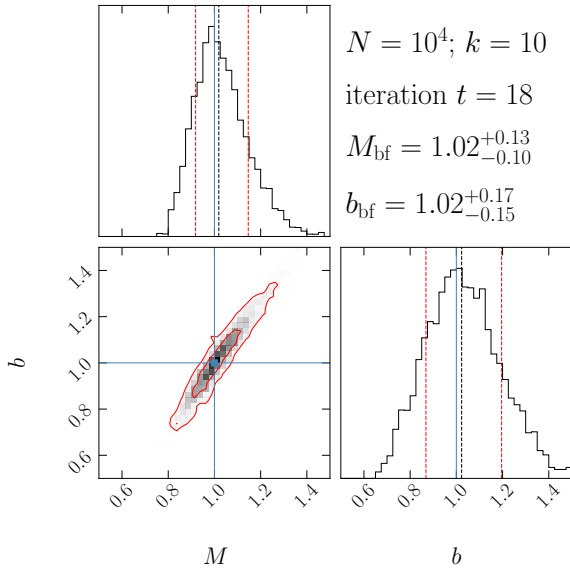


Figure 10. The final posterior on the parameters of the isochrone potential, and respective histograms. This is obtained for a phase-mixed sample of $N \approx 10^4$ particles in an isochrone potential ($M = 1, b = 1$).

entropy estimates in 6D, and in spaces of integrals of motion, i.e. assuming $f = f(E)$, $f = f(E, L)$ or $f = f(\vec{J})$, which are all valid assumptions for the self-consistent sample. Of particular interest, we get a relative error $\delta S_{E,L}/S_{\text{true}} \approx 0.01\%$ for $N = 10^8$ in the (E, L) -space.

We then evolved this same sample in a different Isochrone potential with three times the original mass. From the Jeans theorem, we know that the final DF must be some function $f = f(E, L)$. Since we do not know this $f(E, L)$, the final true entropy cannot be cal-

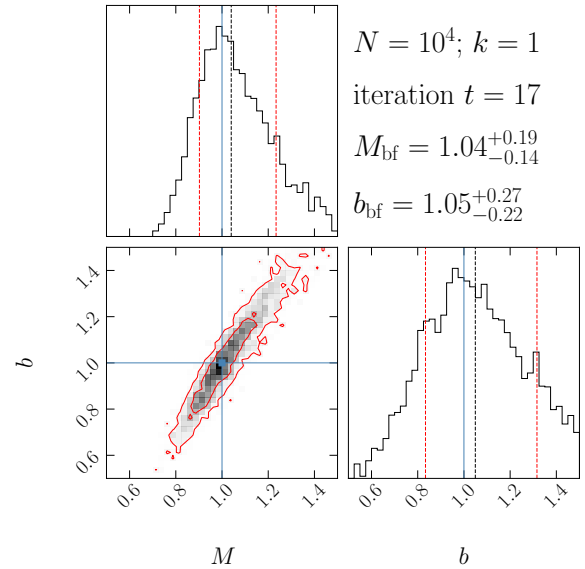


Figure 11. Similar to Fig. 10, but taking the $k = 1$ nearest neighbor in the entropy estimate.

culated with simple integration, but is estimated with $\hat{S}_{E,L}$ with the same expected small error for $N = 10^8$.

Thus, we confidently know the initial and final entropies and conclude that, in order for the system to achieve a stationary state described by the Jeans theorem, *the entropy must increase*. This seems intuitive and in good agreement with the second law of thermodynamics, but it is in sharp contrast with the entropy conservation predicted by the Vlasov equation. This wrong prediction is a consequence of the continuum assumption this equation is based on. Fortunately, real gravitational systems are finite- N and, because of this, evolve towards stationary states constrained by the Jeans theorem.

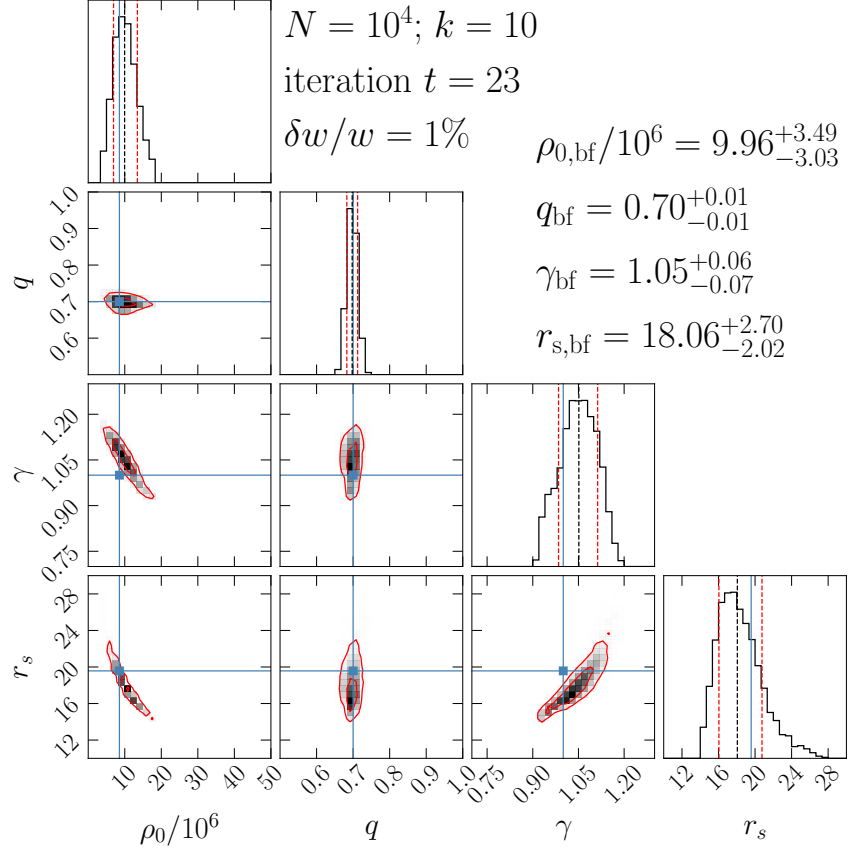


Figure 12. pyABC results for $N = 10^4$ particles that phase-mixed in a flattened axisymmetric potential ($q = 0.7$). Each of the 6D coordinates is assumed to have a Gaussian error distribution with relative uncertainties $\delta w/w = 0.01$. The true parameters (blue lines/dots) are well recovered, except for a small bias in the space of r_s vs γ , which requires further investigation.

It is normally assumed that the relevant time scale for the continuum assumption to be valid is that determining whether the potential is smooth, i.e. the collisional relaxation time $\tau_{\text{col}} \propto (N/\ln N)\tau_{\text{cr}}$, where τ_{cr} is the crossing time. However, the Vlasov equation not only assumes a smooth potential, but it also assumes an infinite number of tracers. The question is whether N is large enough for the latter assumption to hold for the time scales of interest.

The time-scale for phase-mixing to break down this assumption is $\lesssim 0.1N^{1/6}\tau_{\text{cr}} \ll \tau_{\text{col}}$ (Beraldo e Silva et al. 2019b), which is a few crossing times even if we consider samples as large as a whole galaxy with $N \sim 10^{11}$. This collisionless relaxation has its roots on the Nyquist-Shannon theorem (Nyquist 1928; Shannon 1949): in d -dimensions, a size- N sample can only represent functions oscillating with maximum frequencies $k \lesssim N^{1/d}$. Functions oscillating with higher frequencies introduce information not contained in the sample. As shown by Beraldo e Silva et al. (2019a), this theorem constrains the maximum frequency (finest structures) allowed for a DF describing a real, i.e. finite- N , dynamical sys-

tem. The maximum frequency increases linearly with time for integrable systems, and faster for non-integrable ones, until hitting the upper limit set by the Nyquist-Shannon theorem. After that, the system approaches a stationary state constrained by the Jeans theorem, and *does not produce the extra fine phase-space structures predicted by the Vlasov equation*.

This contrasts with the traditional view that the underlying evolution of collisionless systems is governed by the Vlasov equation, while any entropy increase is due to information loss in the measurement process, i.e. coarse-graining (e.g. Lynden-Bell 1967; Tremaine et al. 1986; Dehnen 2005; Levin et al. 2014). Although the work of Dehnen (2005) is the closest to our interpretation, it still assumes that the underlying evolution is described by the Vlasov equation, and that the evolution to a stationary state requires coarse-graining. Besides the reasons given above, the effectiveness of the method presented here and the excellent agreement of the entropy estimates in different spaces of integrals of motion (see Figs.2-3) shows that that is not the case. After all, agreement of estimates in different spaces would require,

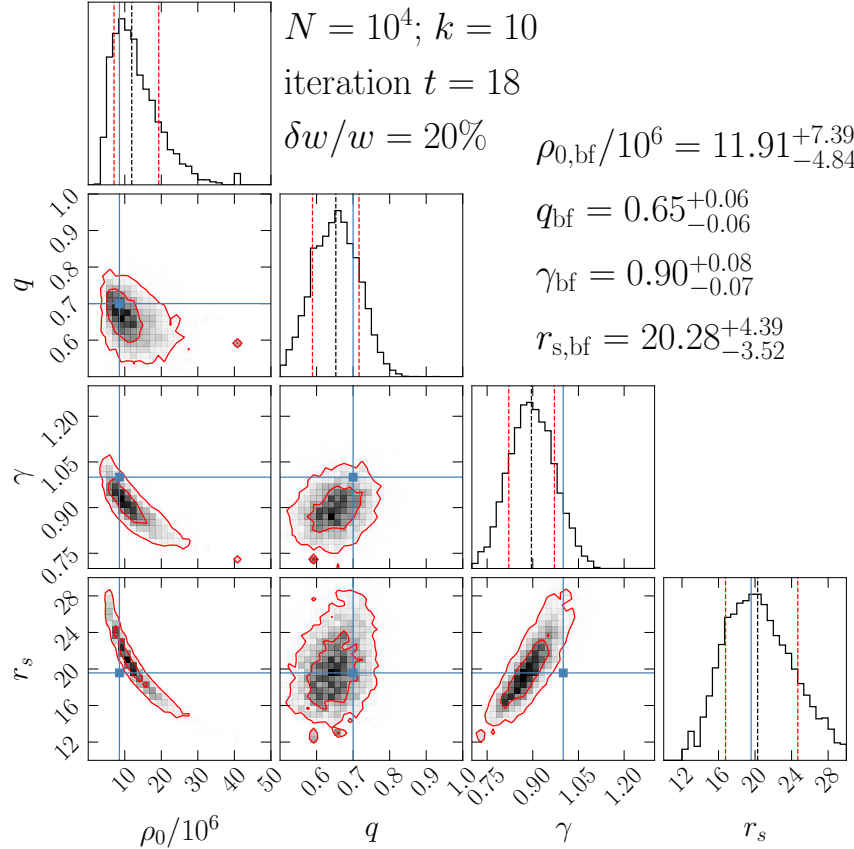


Figure 13. Similar to Fig. 12, but now assuming each coordinate to have Gaussian uncertainties $\delta w/w = 0.2$. We see the worsening of the fit, but the true parameters are still overall well recovered.

if based on coarse-graining, careful choice of the coarse-grain scales, which is not required in our approach.

In summary, the entropy increase considered here is due to a discreteness effect present even in collisionless systems, i.e. in the presence of smooth potentials⁴. We conclude that the method works because it explores an objective entropy increase associated with the phase-mixing of real, i.e. finite- N , collisionless systems.

7.2. Future improvements

An ideal method to constrain a gravitational potential using the kinematics of a stellar sample should:

1. allow constraints on general mass distributions, including general axisymmetric and triaxial systems;
2. properly incorporate uncertainties and covariances in the data, providing not only best fit values, but full probability distributions of the fit parameters;

3. avoid making any assumptions on the DF besides the requirements of the Jeans theorem;
4. be computationally efficient in order to handle samples with $\sim 10^4 - 10^6$ stars, typical of stellar halo samples, or stars within a globular cluster;
5. properly consider the survey’s footprint and selection function;
6. handle incomplete information, e.g. samples missing line-of-sight velocities and/or distances.

We demonstrated that our method already satisfies items 1-4. Although we have not tested it for triaxial potentials, the only difficulty is to efficiently estimate actions in such potentials. This is beyond the scope of the method itself, but with these actions at hand one can also investigate triaxial systems with this method.

Although we demonstrated that the method works, this is not without technical difficulties. In Sec. 4, we discussed the bias and noise associated with the k NN entropy estimator used in this paper. Although this estimator is good enough for most practical applications,

⁴ This is the reason why we refer to the “Vlasov equation” instead of the commonly used “Collisionless Boltzmann Equation”, since the latter can suggest that the evolution of any collisionless system, i.e. one in a smooth potential, is described by this equation.

our method would benefit from more precise and accurate estimates. In the future, it will be important to explore more recent techniques aimed to improve on these estimates – see e.g. Lombardi & Pant (2016); Berrett et al. (2019); Ao & Li (2023) for recent works on this.

In Sec. 4.2, we showed that the bias correction proposed by Charzyńska & Gambin (2015) and implemented here effectively suppressed the bias in the entropy estimates for self-consistent samples of the Isochrone model. This correction assumes a sample whose support is a parallelepiped defined by the extreme values of each coordinate. The typical action-space of a self-consistent sample of an axisymmetric potential has a shape close to a tetrahedron with two perpendicular faces (see Fig. 3.25 in Binney & Tremaine 2008). The reason why this simple correction worked so well in the self-consistent Isochrone sample is probably that this tetrahedron support is not so different from the assumed parallelepiped support for most stars. For non self-consistent samples, and particularly for samples with sharp geometric cuts, the actual support in the action-space can be more complicated. For these cases, it will be important to implement bias corrections that apply to samples with support of a general shape.

The adoption of geometric cuts also introduces selection effects that need to be taken into account when maximizing $\ln \lambda$, Eq. 5. In this case, each star has to be weighted by the probability of finding it in the survey footprint, which is encapsulated in the term A_i . In the DF-fitting method, where one assumes an analytical expression for the DF, $A_i = \int_{\mathcal{V}} f(\vec{w}_i|\vec{p}) \mathbb{S}(\vec{r}_i) d^6 \vec{w}_i$, where \mathcal{V} is the survey volume. This integral can be very complicated and time consuming, and it is the main source of noise in these methods (McMillan & Binney 2013; Hattori et al. 2021). In the minimum-entropy method developed in this paper, we do not have an analytic DF, but A_i can be calculated by computing the fractional time each orbit spends inside the survey footprint. This can be done either by generating a number of angle variables uniformly distributed in $[0, 2\pi)$ for each star and checking how many pairs $(\vec{\theta}, \vec{J})$ end up inside the footprint, or simply integrating orbits and directly counting the fractional time inside the footprint for each orbit.

Other important improvements involve handling unbound stars, such as hyper-velocity stars, and samples with missing data.

7.3. Perturbation from LMC

Complicating the application of this method to the MW is the fact that the Large Magellanic Cloud (LMC) is currently near a pericentric passage (at a distance of ≈ 50 kpc, Besla et al. 2007) and significantly perturbs

the MW halo. This perturbation is significant enough to produce a reflex motion of the MW disc and its inner halo ($\lesssim 30$ kpc) towards the LMC past trajectory (Garavito-Camargo et al. 2021; Petersen & Peñarrubia 2021; Erkal et al. 2021). Thus, dynamical equilibrium cannot be assumed for the outer halo ($\gtrsim 30$ kpc). However, if one wants to probe the outer halo still assuming dynamical equilibrium, a promising avenue is to try to “undo” or correct for the kinematic perturbation from the LMC (Deason et al. 2021; Correa Magnus & Vasiliev 2022). On the other hand, for the inner halo ($\lesssim 30$ kpc) the assumption of equilibrium still seems reasonable.

8. SUMMARY

We have presented a new method to constrain the gravitational potential where a tracer sample is in dynamical equilibrium. This method is based on the idea that, if put in a different potential, this sample would phase-mix, producing an entropy increase. The potential is then recovered by minimizing the entropy of the sample in respect to the parameters of the potential. This entropy is estimated in the space of integrals of motion, and the parameters of the potential enter the fit through these integrals.

We focused on action variables, and demonstrated some of their advantages, including possible constraints on the MW’s DM halo shape. Investigation of this particular problem will benefit from large spectroscopic surveys such as the DESI-MWS (Cooper et al. 2023) in tandem with Gaia. Although our rigorous demonstration shows that the method is strictly valid in action space, in other applications, e.g. in the study of spherical systems like globular clusters, other integrals, such as energy and angular momentum, may also be used.

ACKNOWLEDGMENTS

LBeS thanks Wyn Evans, Josh Speagle, Chirag Modi, David Hogg, Bernardo Modenesi and the stellar halos group at the University of Michigan for useful discussions, and the support provided by the Heising Simons Foundation through the Barbara Pichardo Future Faculty Fellowship from grant # 2022-3927. MV and LBeS acknowledge the support of NASA-ATP award 80NSSC20K0509 and U.S. National Science Foundation AAG grant AST-2009122. EV acknowledges support from an STFC Ernest Rutherford fellowship (ST/X004066/1). KH is supported by JSPS KAKENHI Grant Numbers JP24K07101, JP21K13965, and JP21H00053. WdSP is supported by CNPq (309723/2020-5). KJD acknowledges support provided by the Heising Simons Foundation grant # 2022-3927

Software: numpy (Harris et al. 2020), scipy (Virtanen et al. 2020), Agama (Vasiliev 2019), pyABC (Schälte et al. 2022).

APPENDIX

A. MATHEMATICAL BASIS OF THE MINIMUM-ENTROPY METHOD

In this appendix we demonstrate on mathematical basis why the minimum-entropy works. If the DF describing the sample was separable in the space of angles and actions, i.e. $f(\vec{\theta}, \vec{J}) = \mathcal{F}(\vec{\theta})F(\vec{J})$, the entropy, Eq. (1), would be $S = S_\theta + S_{\mathcal{J}}$, i.e. the sum of the entropies in the respective sub-spaces. Since S is invariant for changes of variables, it is the same for angle-actions evaluated in any potential. In a potential where a sample is in equilibrium, the angle distribution is uniform, $\mathcal{F}(\vec{\theta}) = (2\pi)^{-3}$ and S_θ is maximum. Thus, $S_{\mathcal{J}}$ must be minimum in this potential.

Here we generalize this idea to DFs that are not separable. Incidentally, we also show that, although the method can be applicable to other sets of integrals, it is fully justified and is expected to work better for action variables.

Given the DF $f(\vec{w})$, where $\vec{w} \equiv (\vec{r}, \vec{v})$, consider a random variable $X = (X_1, \dots, X_n)$, with $X_i = X_i(\vec{w})$ – we will later make $X = -\ln f$. Let D_X be the pdf of X , i.e. D_X is a positive function on \mathbb{R}^n . The expectation value of X is

$$\mathbb{E}[X] = \int_{-\infty}^{\infty} X(\vec{w})f(\vec{w}) \, d^6\vec{w} = \int_{-\infty}^{\infty} D_X(\vec{x})\vec{x} \, d^n\vec{x}. \quad (\text{A1})$$

Let $Y = (Y_1, \dots, Y_m)$, with $m < 6$, be a second random variable, with $Y_i = Y_i(\vec{w})$ – we will later make Y be the integrals of motion. We require Y to have the following two properties:

1. There is a smooth function $\Psi : \mathbb{R}^6 \rightarrow \mathbb{R}^6$, whose Jacobian matrix

$$(J_\Psi)_{ij} \doteq \frac{\partial \Psi_i}{\partial w_j}, \quad i, j = 1, \dots, 6$$

is non-degenerate (i.e., its determinant is non-vanishing), such that $Y_k(\vec{w}) = \Psi_k(\vec{w})$, $k = 1, \dots, m$. In other words, Y corresponds to the first $m < 6$ coordinates of some change of variables Ψ in 6D.

2. The Jacobian determinant $|J_\Psi|$ only depends on Y . That is, $|J_\Psi|$ is a function on the space of $\vec{w} = (\vec{r}, \vec{v})$ that only depends on the first m new coordinates defined by Ψ .

Note that requirements 1. and 2. are exactly those met by isolating integrals of motion, e.g.: for spherical and isotropic systems, we set $Y_1 = E$ and we have $|J_\Psi| = g(E)$; for spherical and anisotropic ones, we set $(Y_1, Y_2) = (E, L)$ and we have $|J_\Psi| = g(E, L)$; for angle-action variables, $(Y_1, Y_2, Y_3) = \vec{J}$ and $|J_\Psi| = 1$ – see Secs. 3.1–3.3. In what follows we keep the notation Y for generality but we keep in mind that normally $Y = (Y_1, \dots, Y_m)$ holds m integrals of motion.

For random variables Y respecting 1. and 2., we consider the conditional expectation in the sense of a “disintegration” of f with respect to Y , $(f_y^Y)_{y \in \mathbb{R}^m}$ – for a friendly, yet thorough, introduction to this topic, see Chang & Pollard (1997). This is a family of pdf’s in \mathbb{R}^{6-m} such that for each Y_i , it gives the pdf of the $6 - m$ remaining variables. Note that this is different from marginalizing over remaining variables, and also different from simply fixing values for Y_i and taking f at these fixed values. Formally, f_y^Y is such that, for any random variable X , one has

$$\mathbb{E}(X) = \int_{-\infty}^{\infty} D_Y(\vec{y}) \left\{ \int_{-\infty}^{\infty} f_y^Y(\vec{z}) X[\Psi^{-1}(\vec{y}, \vec{z})] \, d^{6-m}\vec{z} \right\} d^m\vec{y}. \quad (\text{A2})$$

We emphasize that \vec{z} runs over the $6 - m$ remaining variables. Note that if X only depends on Y then

$$\mathbb{E}(X) = \int_{-\infty}^{\infty} D_Y(\vec{y}) X(\vec{y}) \, d^m\vec{y}, \quad (\text{A3})$$

where $X(\vec{y}) = X(Y = \vec{y})$. If $|J_\Psi| = |J_\Psi|(Y)$, the disintegration of f with respect to Y is explicitly given by:

$$f_y^Y(\vec{z}) = \frac{f[\Psi^{-1}(\vec{y}, \vec{z})]}{\int_{-\infty}^{\infty} f[\Psi^{-1}(\vec{y}, \vec{z}')] \, d^{6-m}\vec{z}'},$$

and thus

$$f[\Psi^{-1}(\vec{y}, \vec{z})] = \left\{ \int_{-\infty}^{\infty} f[\Psi^{-1}(\vec{y}, \vec{z}')] d^{6-m} \vec{z}' \right\} f_y^Y(\vec{z}). \quad (\text{A4})$$

In fact, in this case,

$$\begin{aligned} \mathbb{E}(X) &= \int_{-\infty}^{\infty} X(\vec{w}) f(\vec{w}) d^6 \vec{w} = \int_{-\infty}^{\infty} X[\Psi^{-1}(\vec{y}, \vec{z})] f[\Psi^{-1}(\vec{y}, \vec{z})] |J_{\Psi}(\vec{y})| d^m \vec{y} d^{6-m} \vec{z} \\ &= \int_{-\infty}^{\infty} \left\{ \int_{-\infty}^{\infty} f[\Psi^{-1}(\vec{y}, \vec{z}')] d^{6-m} \vec{z}' \right\} |J_{\Psi}(\vec{y})| \left\{ \frac{f[\Psi^{-1}(\vec{y}, \vec{z})]}{\int_{-\infty}^{\infty} f[\Psi^{-1}(\vec{y}, \vec{z}')] d^{6-m} \vec{z}'} \right\} X[\Psi^{-1}(\vec{y}, \vec{z})] d^m \vec{y} d^{6-m} \vec{z} \\ &= \int_{-\infty}^{\infty} D_Y(\vec{y}) \left\{ \int_{-\infty}^{\infty} f_y^Y(\vec{z}) X[\Psi^{-1}(\vec{y}, \vec{z})] d^{6-m} \vec{z} \right\} d^m \vec{y}, \end{aligned}$$

with

$$D_Y(\vec{y}) = \left\{ \int_{-\infty}^{\infty} f[\Psi^{-1}(\vec{y}, \vec{z}')] d^{6-m} \vec{z}' \right\} |J_{\Psi}(\vec{y})|$$

being the density of the random variable Y . In particular, by Eq. (A4),

$$f[\Psi^{-1}(\vec{y}, \vec{z})] = \frac{D_Y(\vec{y}) f_y^Y(\vec{z})}{|J_{\Psi}(\vec{y})|}. \quad (\text{A5})$$

Making $X = -\ln f$ in Eqs. (A2), (A3) and (A5), we get the following expression for the entropy $S(f)$ in terms of the entropy $S(D_Y)$ of the pdf D_Y and $S(f_y^Y)$, the entropies of the pdf's on \mathbb{R}^{6-m} appearing in the disintegration of f :

$$\begin{aligned} S(f) &= \mathbb{E}(-\ln f) = \int_{-\infty}^{\infty} D_Y(\vec{y}) \left\{ \int_{-\infty}^{\infty} f_y^Y(\vec{z}) [-\ln f(\Psi^{-1}(\vec{y}, \vec{z}))] d^{6-m} \vec{z} \right\} d^m \vec{y} \\ &= \int_{-\infty}^{\infty} D_Y(\vec{y}) \left\{ \int_{-\infty}^{\infty} f_y^Y(\vec{z}) \left[-\ln \left(\frac{D_Y(\vec{y}) f_y^Y(\vec{z})}{|J_{\Psi}(\vec{y})|} \right) \right] d^{6-m} \vec{z} \right\} d^m \vec{y} \\ &= \int_{-\infty}^{\infty} D_Y(\vec{y}) \left\{ \int_{-\infty}^{\infty} f_y^Y(\vec{z}) [\ln |J_{\Psi}(\vec{y})| - \ln D_Y(\vec{y}) - \ln f_y^Y(\vec{z})] d^{6-m} \vec{z} \right\} d^m \vec{y} \\ &= \int_{-\infty}^{\infty} D_Y(\vec{y}) \ln |J_{\Psi}(\vec{y})| d^m \vec{y} + \int_{-\infty}^{\infty} D_Y(\vec{y}) [-\ln D_Y(\vec{y})] d^m \vec{y} \\ &\quad + \int_{-\infty}^{\infty} D_Y(\vec{y}) \left\{ \int_{-\infty}^{\infty} f_y^Y(\vec{z}) [-\ln f_y^Y(\vec{z})] d^{6-m} \vec{z} \right\} d^m \vec{y} \\ &= \mathbb{E}(\ln |J_{\Psi}|) + S(D_Y) + \int_{-\infty}^{\infty} D_Y(\vec{y}) S(f_y^Y) d^m \vec{y}. \end{aligned}$$

Hence,

$$S(f) = \mathbb{E}(\ln |J_{\Psi}|) + S(D_Y) + \mathbb{E} \left(S(f_{(\cdot)}^Y) \right), \quad (\text{A6})$$

where $\mathbb{E} \left(S(f_{(\cdot)}^Y) \right)$ denotes the expectation of the entropy $S(f_y^Y)$ of the pdf's in the disintegration of f with respect to Y . Note that these entropies define a random variable $S(f_{(\cdot)}^Y)$ that only depends on Y . In particular, if Ψ is a canonical transformation, the following identity holds:

$$S(f) = S(D_Y) + \mathbb{E} \left(S(f_{(\cdot)}^Y) \right).$$

Eq. (A6) is the main result of this appendix. We show now that it justifies our minimum-entropy method for fitting galactic potentials. Consider a family Ψ_i , $i \in I$, of transformations of coordinates in \mathbb{R}^6 , where I is an index set. More specifically, we think of Ψ_i as the set of transformations of variables leading to integrals of motion evaluated in all trial

potentials. For some fixed $m < 6$, define Y_i , $i \in I$, by the m first components of Ψ_i , as above. Suppose that, for all $i \in I$ and $\vec{y} \in \mathbb{R}^m$, the pdf's $f_y^{Y_i}$ are supported in some bounded region Ω_z of \mathbb{R}^{6-m} , which does not depend on $\vec{y} \in \mathbb{R}^m$ or on $i \in I$. In fact, if we use angle-action variables $(\vec{\theta}, \vec{J})$ and set $Y = \vec{J}$, the support Ω_z of the remaining variables neither depends on $\vec{y} \in \mathbb{R}^m$ nor on the potential, since the support of each angle variable is always $[0, 2\pi)$. In this case, the third term in the right-hand side of Eq. (A6) assumes its maximum value for uniform distributions on the remaining variables. This property does not necessarily hold when we use different sets of integrals of motion, which then advocates for the use of actions, as also suggested by their better results in comparison to using $S_{E,L}$ – compare Figs 6 and 7. This is so even with the fluctuation and bias of the entropy estimates being worse at higher dimensions.

Furthermore, assume that, for some $i_0 \in I$, i.e. for some potential, f “only depends on Y_{i_0} ”, by which we mean that, for all $\vec{y} \in \mathbb{R}^m$, the (disintegrated) pdf $f_y^{Y_{i_0}}$ is constant within its support Ω_z . *This last property refers to Jeans theorem.* It should be noted that, strictly speaking, $f_y^{Y_{i_0}}$ does depend on $\vec{z} \in \mathbb{R}^{6-m}$, because $f_y^{Y_{i_0}}$ switches from zero to some positive value when \vec{z} is moved from outside the support Ω_z to its interior. This is why we employed quotation marks. Recalling that a pdf supported on a fixed bounded region of \mathbb{R}^{6-m} has maximal entropy if it is uniform, $f_y^{Y_i}$ is uniform on its support for all $\vec{y} \in \mathbb{R}^m$ only if $\mathbb{E}\left(S(f_{(\cdot)}^{Y_i})\right)$ attains its maximum with respect to $i \in I$. Consequently, in this case the quantity $\mathbb{E}(\ln |J_{Y_i}|) + S(D_{Y_i})$ is minimum, as $S(f)$ does not depend on $i \in I$, i.e. $S(f)$ is invariant for changes of variables. Thus, the index $i_0 \in I$ with the above particular property can be found by minimizing $\mathbb{E}(\ln |J_{Y_i}|) + S(D_{Y_i})$ with respect to i in the index set I , i.e. among the potentials. If Ψ_i , $i \in I$, is a family of canonical transformations one simply minimizes $S(D_{Y_i})$, the differential entropy of the density of the m first coordinates of Ψ_i .

REFERENCES

- Akaike, H. 1992, Information Theory and an Extension of the Maximum Likelihood Principle (New York, NY: Springer New York), 610–624, doi: [10.1007/978-1-4612-0919-5_38](https://doi.org/10.1007/978-1-4612-0919-5_38)
- Ao, Z., & Li, J. 2023, Artificial Intelligence, 322, 103954, doi: <https://doi.org/10.1016/j.artint.2023.103954>
- Bahcall, J. N., & Tremaine, S. 1981, ApJ, 244, 805, doi: [10.1086/158756](https://doi.org/10.1086/158756)
- Beaumont, M. A., Zhang, W., & Balding, D. J. 2002, Genetics, 162, 2025, doi: [10.1093/genetics/162.4.2025](https://doi.org/10.1093/genetics/162.4.2025)
- Beirlant, J., Dudewicz, E., Gyor, L., & Meulen, E. 1997, International Journal of Mathematical and Statistical Sciences, 6
- Beloborodov, A. M., & Levin, Y. 2004, ApJ, 613, 224, doi: [10.1086/422908](https://doi.org/10.1086/422908)
- Beraldo e Silva, L., de Siqueira Pedra, W., Sodr e, L., Perico, E. L. D., & Lima, M. 2017, ApJ, 846, 125, doi: [10.3847/1538-4357/aa876e](https://doi.org/10.3847/1538-4357/aa876e)
- Beraldo e Silva, L., de Siqueira Pedra, W., & Valluri, M. 2019a, ApJ, 872, 20, doi: [10.3847/1538-4357/aaf8a7](https://doi.org/10.3847/1538-4357/aaf8a7)
- Beraldo e Silva, L., de Siqueira Pedra, W., Valluri, M., Sodr e, L., & Bru, J.-B. 2019b, ApJ, 870, 128, doi: [10.3847/1538-4357/aaf397](https://doi.org/10.3847/1538-4357/aaf397)
- Berrett, T. B., Samworth, R. J., & Yuan, M. 2019, The Annals of Statistics, 47, pp. 288
- Besla, G., Kallivayalil, N., Hernquist, L., et al. 2007, ApJ, 668, 949, doi: [10.1086/521385](https://doi.org/10.1086/521385)
- Biau, G., & Devroye, L. 2015, Lectures on the Nearest Neighbor Method, 1st edn. (Springer Publishing Company, Incorporated)
- Binney, J. 2012, MNRAS, 426, 1324, doi: [10.1111/j.1365-2966.2012.21757.x](https://doi.org/10.1111/j.1365-2966.2012.21757.x)
- Binney, J., & Petrou, M. 1985, MNRAS, 214, 449, doi: [10.1093/mnras/214.4.449](https://doi.org/10.1093/mnras/214.4.449)
- Binney, J., & Tremaine, S. 2008, Galactic Dynamics: Second Edition, Princeton Series in Astrophysics (Princeton University Press)
- Chang, J. T., & Pollard, D. 1997, Statistica Neerlandica, 51, 287, doi: <https://doi.org/10.1111/1467-9574.00056>
- Charzyńska, A., & Gambin, A. 2015, Entropy, 18, 13, doi: [10.3390/e18010013](https://doi.org/10.3390/e18010013) FILE:/proj/ads/abstracts/
- Cooper, A. P., Koposov, S. E., Allende Prieto, C., et al. 2023, ApJ, 947, 37, doi: [10.3847/1538-4357/acb3c0](https://doi.org/10.3847/1538-4357/acb3c0)
- Correa Magnus, L., & Vasiliev, E. 2022, MNRAS, 511, 2610, doi: [10.1093/mnras/stab3726](https://doi.org/10.1093/mnras/stab3726)
- Cranmer, K., Brehmer, J., & Louppe, G. 2020, Proceedings of the National Academy of Science, 117, 30055, doi: [10.1073/pnas.1912789117](https://doi.org/10.1073/pnas.1912789117)
- Cui, X.-Q., Zhao, Y.-H., Chu, Y.-Q., et al. 2012, Research in Astronomy and Astrophysics, 12, 1197, doi: [10.1088/1674-4527/12/9/003](https://doi.org/10.1088/1674-4527/12/9/003)
- De Silva, G. M., Freeman, K. C., Bland-Hawthorn, J., et al. 2015, MNRAS, 449, 2604, doi: [10.1093/mnras/stv327](https://doi.org/10.1093/mnras/stv327)
- Deason, A. J., Erkal, D., Belokurov, V., et al. 2021, MNRAS, 501, 5964, doi: [10.1093/mnras/staa3984](https://doi.org/10.1093/mnras/staa3984)

- Dehnen, W. 2005, *MNRAS*, 360, 892, doi: [10.1111/j.1365-2966.2005.09099.x](https://doi.org/10.1111/j.1365-2966.2005.09099.x)
- Erkal, D., Deason, A. J., Belokurov, V., et al. 2021, *MNRAS*, 506, 2677, doi: [10.1093/mnras/stab1828](https://doi.org/10.1093/mnras/stab1828)
- Evans, N. W., & An, J. 2005, *MNRAS*, 360, 492, doi: [10.1111/j.1365-2966.2005.09078.x](https://doi.org/10.1111/j.1365-2966.2005.09078.x)
- Gaia Collaboration, et al. 2016, *A&A*, 595, A1, doi: [10.1051/0004-6361/201629272](https://doi.org/10.1051/0004-6361/201629272)
- Garavito-Camargo, N., Besla, G., Laporte, C. F. P., et al. 2021, *ApJ*, 919, 109, doi: [10.3847/1538-4357/ac0b44](https://doi.org/10.3847/1538-4357/ac0b44)
- Green, G. M., Ting, Y.-S., & Kamdar, H. 2023, *ApJ*, 942, 26, doi: [10.3847/1538-4357/aca3a7](https://doi.org/10.3847/1538-4357/aca3a7)
- Hahn, C., Vakili, M., Walsh, K., et al. 2017, *MNRAS*, 469, 2791, doi: [10.1093/mnras/stx894](https://doi.org/10.1093/mnras/stx894)
- Han, J., Wang, W., Cole, S., & Frenk, C. S. 2016, *MNRAS*, 456, 1003, doi: [10.1093/mnras/stv2707](https://doi.org/10.1093/mnras/stv2707)
- Harris, C. R., Millman, K. J., van der Walt, S. J., et al. 2020, *Nature*, 585, 357, doi: [10.1038/s41586-020-2649-2](https://doi.org/10.1038/s41586-020-2649-2)
- Hattori, K., Valluri, M., & Vasiliev, E. 2021, *MNRAS*, 508, 5468, doi: [10.1093/mnras/stab2898](https://doi.org/10.1093/mnras/stab2898)
- Henon, M. 1959, *Annales d'Astrophysique*, 22, 126
- Hernquist, L. 1990, *ApJ*, 356, 359, doi: [10.1086/168845](https://doi.org/10.1086/168845)
- Jiang, B. 2018, in *Proceedings of Machine Learning Research*, Vol. 84, *Proceedings of the Twenty-First International Conference on Artificial Intelligence and Statistics*, ed. A. Storkey & F. Perez-Cruz (PMLR), 1711–1721. <https://proceedings.mlr.press/v84/jiang18a.html>
- Kullback, S. 1968, *Information theory and statistics* (Dover publications)
- Leonenko, N., Pronzato, L., & Savani, V. 2008, *The Annals of Statistics*, 36, 2153, doi: [10.1214/07-AOS539](https://doi.org/10.1214/07-AOS539)
- Levin, Y., Pakter, R., Rizzato, F. B., Teles, T. N., & Benetti, F. P. C. 2014, *PhR*, 535, 1, doi: [10.1016/j.physrep.2013.10.001](https://doi.org/10.1016/j.physrep.2013.10.001)
- Lombardi, D., & Pant, S. 2016, *PhRvE*, 93, 013310, doi: [10.1103/PhysRevE.93.013310](https://doi.org/10.1103/PhysRevE.93.013310)
- Lynden-Bell, D. 1967, *MNRAS*, 136, 101, doi: [10.1093/mnras/136.1.101](https://doi.org/10.1093/mnras/136.1.101)
- Magorrian, J. 2014, *MNRAS*, 437, 2230, doi: [10.1093/mnras/stt2031](https://doi.org/10.1093/mnras/stt2031)
- Majewski, S. R., Schiavon, R. P., Frinchaboy, P. M., et al. 2017, *AJ*, 154, 94, doi: [10.3847/1538-3881/aa784d](https://doi.org/10.3847/1538-3881/aa784d)
- Martin, O., Kumar, R., & Lao, J. 2021, *Bayesian Modeling and Computation in Python*, Chapman & Hall/CRC Texts in Statistical Science (CRC Press). <https://books.google.com/books?id=0UtSEAAAQBAJ>
- McMillan, P. J. 2017, *MNRAS*, 465, 76, doi: [10.1093/mnras/stw2759](https://doi.org/10.1093/mnras/stw2759)
- McMillan, P. J., & Binney, J. 2012, *MNRAS*, 419, 2251, doi: [10.1111/j.1365-2966.2011.19879.x](https://doi.org/10.1111/j.1365-2966.2011.19879.x)
- McMillan, P. J., & Binney, J. J. 2013, *MNRAS*, 433, 1411, doi: [10.1093/mnras/stt814](https://doi.org/10.1093/mnras/stt814)
- Nyquist, H. 1928, *Transactions of the American Institute of Electrical Engineers*, 47, 617, doi: [10.1109/T-AIEE.1928.5055024](https://doi.org/10.1109/T-AIEE.1928.5055024)
- Peñarrubia, J., Kuposov, S. E., & Walker, M. G. 2012, *ApJ*, 760, 2, doi: [10.1088/0004-637X/760/1/2](https://doi.org/10.1088/0004-637X/760/1/2)
- Petersen, M. S., & Peñarrubia, J. 2021, *Nature Astronomy*, 5, 251, doi: [10.1038/s41550-020-01254-3](https://doi.org/10.1038/s41550-020-01254-3)
- Plummer, H. C. 1911, *MNRAS*, 71, 460, doi: [10.1093/mnras/71.5.460](https://doi.org/10.1093/mnras/71.5.460)
- Sanders, J. L., & Binney, J. 2016, *MNRAS*, 457, 2107, doi: [10.1093/mnras/stw106](https://doi.org/10.1093/mnras/stw106)
- Sanderson, R. E., Helmi, A., & Hogg, D. W. 2015, *ApJ*, 801, 98, doi: [10.1088/0004-637X/801/2/98](https://doi.org/10.1088/0004-637X/801/2/98)
- Schälte, Y., Klinger, E., Alamoudi, E., & Hasenauer, J. 2022, *Journal of Open Source Software*, 7, 4304, doi: [10.21105/joss.04304](https://doi.org/10.21105/joss.04304)
- Shannon, C. 1949, *Proceedings of the IRE*, 37, 10, doi: [10.1109/JRPROC.1949.232969](https://doi.org/10.1109/JRPROC.1949.232969)
- Silverman, B. W. 1986, *Density estimation for statistics and data analysis* (Chapman and Hall)
- Sisson, S., Fan, Y., & Beaumont, M. 2018, *Handbook of Approximate Bayesian Computation*, ISSN (CRC Press)
- Sisson, S. A., Fan, Y., & Tanaka, M. M. 2007, *Proceedings of the National Academy of Sciences*, 104, 1760, doi: [10.1073/pnas.0607208104](https://doi.org/10.1073/pnas.0607208104)
- Ting, Y.-S., Rix, H.-W., Bovy, J., & van de Ven, G. 2013, *MNRAS*, 434, 652, doi: [10.1093/mnras/stt1053](https://doi.org/10.1093/mnras/stt1053)
- Tremaine, S. 2018, *MNRAS*, 477, 946, doi: [10.1093/mnras/sty737](https://doi.org/10.1093/mnras/sty737)
- Tremaine, S., Henon, M., & Lynden-Bell, D. 1986, *MNRAS*, 219, 285, doi: [10.1093/mnras/219.2.285](https://doi.org/10.1093/mnras/219.2.285)
- Trick, W. H., Bovy, J., & Rix, H.-W. 2016, *ApJ*, 830, 97, doi: [10.3847/0004-637X/830/2/97](https://doi.org/10.3847/0004-637X/830/2/97)
- Valluri, M., Chabanier, S., Irsic, V., et al. 2022, *arXiv e-prints*, arXiv:2203.07491, doi: [10.48550/arXiv.2203.07491](https://doi.org/10.48550/arXiv.2203.07491)
- Vasiliev, E. 2019, *MNRAS*, 482, 1525, doi: [10.1093/mnras/sty2672](https://doi.org/10.1093/mnras/sty2672)
- Virtanen, P., Gommers, R., Oliphant, T. E., et al. 2020, *Nature Methods*, 17, 261, doi: [10.1038/s41592-019-0686-2](https://doi.org/10.1038/s41592-019-0686-2)
- Watkins, L. L., Evans, N. W., & An, J. H. 2010, *MNRAS*, 406, 264, doi: [10.1111/j.1365-2966.2010.16708.x](https://doi.org/10.1111/j.1365-2966.2010.16708.x)
- Wolsztynski, E., Thierry, E., & Pronzato, L. 2005, *Signal Processing*, 85, 937, doi: <https://doi.org/10.1016/j.sigpro.2004.11.028>
- Zwicky, F. 1933, *Helvetica Physica Acta*, 6, 110